

Discontinuous control-volume/finite-element method for advection-diffusion problems

G. Stipcich^{*,a,1}, M. Piller^a, M. Pivetta^b, L. Zovatto^a

^a*Università degli Studi di Trieste, Dipartimento di Ingegneria Civile e Ambientale,
via A. Valerio 10, 34127 Trieste, Italy*

^b*Università degli Studi di Trieste, Dipartimento di Matematica e Informatica,
via A. Valerio 12/1, 34127 Trieste, Italy*

Abstract

The discontinuous control-volume/finite-element method is applied to the one-dimensional advection-diffusion equation. The aforementioned methodology is relatively novel and has been mainly applied for the solution of pure-advection problems. This work focuses on the main features of an accurate representation of the diffusion operator, which are investigated both by Fourier analysis and numerical experiments. A *mixed formulation* is followed, where the constitutive equation for the diffusive flux is not substituted into the conservation equation for the transported scalar. The Fourier analysis of a linear, diffusion problem shows that the resolution error is both dispersive and dissipative, in contrast with the purely dissipative error of the traditional continuous Galerkin approximation.

Key words: CVFEM, spectral methods, discontinuous methods, advection-diffusion, mixed formulation

1. Introduction

In the framework of the finite-element method, there are many workable choices of weight functions, the Galerkin method being one of the most successful. An alternative method that has gained some importance in recent

*Corresponding author

Email addresses: `goran.stipcich@phd.units.it` (G. Stipcich), `pillier@units.it` (M. Piller)

¹*tel:* +39 040 558 7896, *fax:* +39 040 558 3497

years, mainly for fluid dynamics and heat transfer applications, is the control-volume/finite-element method (CVFEM hereafter), where volume indicator distributions are chosen as weight functions [33]. One of the first applications of the CVFEM method to advection-diffusion problems in two dimensions is reported by Baliga and Patankar [4]. The discrete equations are obtained by deriving algebraic approximations to integral conservation equations applied to polygonal control volumes, built around each node of a triangular mesh. The method is reported to possess several attractive features, as the geometrical flexibility, the inherent satisfaction of local conservation, an easy physical interpretation. Schneider and Raw [41] devise an upwinding procedure for control-volume-based finite-element convection-diffusion computations and apply the proposed method with bilinear, quadrilateral elements. The authors mention the intrinsic geometric flexibility of the method, inherited from finite elements, and the *direct physical invocation of a conservation principle to clearly identified and delineated control volumes*, as remarkable appealing features of the CVFEM approach. Banaszek [5] carries out a detailed analysis of consistent and lumped versions of CVFEM and Galerkin finite-element (GFEM hereafter) algorithms for diffusion-type problems. Banaszek [5] investigates the properties of bilinear, quadrilateral elements, nine-node (Lagrange) quadrilateral elements, eight-node Serendipity elements and six-node triangular elements. Banaszek [5] points out some of the positive characteristics of the CVFEM approach, for the considered class of problems: local conservation is achieved at control volume level, superior accuracy and stability for CVFEM with respect to GFEM and preservation of the discrete maximum principle [12]. According to Banaszek [5], the superiority of CVFEM over the GFEM is not as definitive for advection-diffusion problems. Giannakouros and Karniadakis [16, 17] and Sidilkover and Karniadakis [42] propose an original spectral CVFEM algorithm for hyperbolic conservation equations and for the compressible Euler equations, exploiting high-order interpolating shape functions. A one-dimensional, staggered grid of Gauss-Chebyshev and Gauss-Chebyshev-Lobatto collocation points is employed to accommodate the control-volume averages and point values within each element. The cell averages are the main unknowns, while the point values are obtained from the cell averages using appropriate reconstruction procedures and are used for the calculation of the advective fluxes at the boundaries of the control volumes. Masson et al. [34] devise a primitive-variable, co-located, equal-order CVFEM formulation for the axis-symmetric, incompressible Navier-Stokes equations with heat transfer. Three-node tri-

angular elements, embedding linear shape functions for the representation of all dependent variables, define the computational mesh on a longitudinal cross-plane.

Discontinuous methods were developed at first in the finite-element framework. The resulting *discontinuous Galerkin* methods (DGFEM hereafter), as opposed to the continuous Galerkin approach (GFEM), are characterized by the relaxation of the continuity constraint between neighboring elements, which is imposed in weak form through the so called *numerical fluxes* [26] or *numerical traces* [14]. Each DGFEM differs by the specific definition of numerical fluxes, which strongly affect the consistency, stability and accuracy of the method [14]. The first DGFEM formulation for hyperbolic equations is ascribed to Reed and Hill [39], opening the way for an active development of DGFEM algorithms for hyperbolic and nearly hyperbolic equations. In the 1970s several DGFEMs for elliptic and parabolic problems are proposed, referred to as *interior penalty methods* [3, 9]. More recently an approach for elliptic equations is introduced by Bassi and Rebay [6] and some variations studied by Brezzi et al. [8]. A generalization called *local discontinuous Galerkin method* (LDG), introduced by Cockburn and Shu [13], applies to the system of first-order equations formed by the constitutive and conservation equations, rather than considering the *fundamental equation* resulting from their combination. The *recovery method* is proposed by van Leer and Lo [25] as an alternative computation of the numerical fluxes in a DGFEM scheme for diffusion. The elements' coupling is obtained by fitting a $2N$ degree polynomial through the elements' interface, where N is the degree of the polynomial used within the single element. van Leer and Lo [25] propose a DGFEM approach for quadrilateral and triangular elements, where the modal expansion within elements is based on Legendre polynomials. Non-orthogonal, interpolating polynomials are used to calculate the numerical fluxes. Liu and Yan [28, 29] introduce a *direct* discontinuous Galerkin (DDG) method for convection-diffusion problems, based on a consistent and conservative representation of numerical fluxes. DDG applies directly to the *fundamental* equation. A consistent and conservative general numerical flux formula for the solution derivative is proposed.

The discontinuous philosophy has been applied within the CVFEM framework [11, 20], giving rise to discontinuous control-volume/finite-element methods (DCVFEM - hereafter). Research in this area is mainly focused on hyperbolic problems [11, 20]. Iskandarani et al. [20] provide a thorough comparison of spectral GFEM, Taylor-Galerkin Least Square finite elements

(TGLS), DGFEM and DCVFEM for the linear advection equation, using quadrilateral elements with interpolating polynomials of degree four to nine. The interpolation points within each element, in transformed space, are located at N Gauss-Legendre quadrature nodes while the control-volume edges lie on $N + 1$ Gauss-Lobatto-Legendre quadrature nodes. Fourier analysis is not used to reveal the peculiar features of each methodology. Numerical evidence shows that the spectral-GFEM method is the most efficient provided the solution is smooth and well resolved on the computational grid. The coarse-grid simulation of the advection of a passive tracer in a complex velocity field (Hecht problem [18]), where it undergoes severe shearing and straining, shows that the spectral-FEM and TGLS results are severely affected by Gibbs oscillations in under-resolved regions. The DGFEM approach damps the grid-scale noise without affecting the large-scale structure ([20], p. 250). Choi et al. [11] apply the DCVFEM method to the shallow water equations, using quadrilateral elements. The same distribution of interpolation points and control-volume edges is adopted, as used by Iskandarani et al. [20]. The numerical fluxes at inter-element boundaries are computed by a flux-corrected transport (FCT) algorithm [54]. The smooth solutions of two linearized problems exhibit a convergence order of $N + 2$, where the polynomial order of interpolation within elements is N .

The spectral volume method (SV hereafter) is a high-order, discontinuous, finite volume method, originally developed by Wang [49] for hyperbolic conservation laws on two-dimensional, triangular, unstructured grids [30, 49–53]. Since then, SV has been successfully applied for the solution of the Euler [52] and Maxwell [30] equations. The SV approximation of the viscous fluxes in the Navier-Stokes equations is tackled by Sun et al. [45] by an LDG approach. Different representations of the diffusive fluxes have been investigated by Fourier analysis and numerical tests, as the penalty and BR2 approaches [21] and unoptimized as well as optimized variants of the DDG method [22]. Van den Abeele et al. [47] use the Fourier analysis to investigate the wave propagation properties of the one-dimensional SV. Different flux formulations are compared for the solution of the Navier Stokes equations by Kannan and Wang [21, 23]. New formulations of the numerical fluxes, a variant of the interior penalty method of Bassi and Rebay [6] and a variant of the LDG, referred to as LDG2, are proposed by Kannan and Wang [21] and Kannan and Wang [23], respectively.

SV shares several features with the DGFEM and DCVFEM, such as discontinuous solution space, compact support for the approximations, $h - p$

refinement capability. The major difference between the SV and DGFEM or DCVFEM lies in the definition of the unknown degrees of freedom, which for SV are control-volume-averaged values, while in DGFEM and DCVFEM are (interpolating) nodal values or, in the case of hierarchical modal expansions (in DGFEM), expansion modes. In addition, both the DGFEM and DCVFEM approximations of conservation laws require both volume and surface integrations, while SVM requires surface integrations followed by a reconstruction procedure, used to derive point values from control-volume-averaged values [49]. Another significant difference can be identified in the kind of tessellations used to partition the computational domain. The proposed SV approaches use simplex elements (triangles in 2D, tetrahedrons in 3D), further subdivided into a *structured pattern of subcells* [22], whose number and shape depend on the degree of polynomial reconstruction. DGFEM may exploit the whole multiplicity of elements, used in continuous FEM [26]. To the authors' best knowledge, so far DCVFEM has been proposed only with *bar* and quadrilateral elements [20, 33], as these types of elements may be subdivided very naturally into control volumes.

The spectral difference (SD) method, originally formulated by Liu et al. [31], shares with DG and SV methods the use of piecewise continuous functions as the solution approximation space, and the capability of achieving high order accuracy on an unstructured mesh having a compact stencil [36, 47]. The solutions between two different cells are coupled using Riemann solvers [47]. An advantage of SD method over DG and SV is that no integrals are involved in computing the residuals, thus avoiding the costly high-order quadrature formulas. SD is recently used by Parsani et al. [36] for large eddy simulation (LES) in 2D, using quadrilateral cells and treating the diffusive terms with the BR2 approach of Bassi and Rebay [7].

Fourier analysis is a widely-used approach for investigating the accuracy, stability and resolutions characteristics of high-order methods. Zhang and Shu [55] use Fourier analysis to provide the order of accuracy and to establish the stability or instability of three different DG semi-discretizations for the diffusion equation. Kannan and Wang [21] propose an interior penalty approach for the numerical viscous fluxes, resulting from a SVM discretization of the Navier-Stokes equations. Fourier analysis is used to compare the proposed formulation with the LDG approach. In Kannan and Wang [23], Fourier analysis is used to study the resolution properties of the proposed LDG2 formulation for the numerical fluxes, for the SVM semi-discretization of the one-dimensional diffusion equation. The analysis focuses on the lin-

ear, quadratic and cubic polynomial reconstructions. Kannan and Wang [22] propose two novel DDG methods [28] in the SVM framework and use Fourier analysis to compare the dissipation properties of the proposed schemes with existing flux formulations for the 1D diffusion equation. Van den Abeele et al. [46] analyze the dispersive and dissipative properties of the spatial discretization of the one-dimensional transport equation by the SV method. The approach followed is completely analogous to the one in [19]. Fourier analysis is also used to derive the stability characteristics of the SV method, when the time-discretization is carried out by different versions of Runge-Kutta schemes, including a TVD Runge-Kutta scheme [43].

The present work provides a one-dimensional extension of the spectral-DCVFEM method to diffusion-dominated and advection-diffusion problems. The mixed formulation is used [56, ch.11,12], where both the transported scalar field and the associated diffusive flux are considered as dependent quantities. The mixed formulation is used to achieve an accurate approximation of both the scalar quantity and the corresponding flux, to relax the regularity requirements on the depending variables [15] and to derive locally conservative finite-element formulations. Integrating both the conservation and the constitutive equations over control-volumes, which are entirely contained within elements, gives rise to inter-element (or *numerical*) fluxes, which, in the present work, are represented by the LDG formulation by Cockburn and Shu [13]. A formal derivation of the proposed DCVFEM is provided. The accuracy and resolution capabilities of the proposed numerical scheme are investigated by Fourier analysis, which reveals some peculiar features of the method. Numerical simulations of selected problems are used to confirm the theoretical results and to investigate additional characteristics of the proposed methodology. Although the present work focuses on the development of the discontinuous finite-volume algorithm for the one-dimensional advection-diffusion equation, the method is formulated in a rather general framework, which can be applied also in two and three dimensions. This is demonstrated in section 5.4, where the steady-state, two-dimensional diffusion problem with source term is solved numerically, using quadrilateral elements.

2. Governing equations

A formal derivation of the mixed formulation for DCVFEM is provided. The multidimensional form of the equations is considered.

2.1. Strong formulation

The scalar advection-diffusion conservation principle can be cast as

$$\begin{cases} \mathbf{q}_d + D \nabla T = 0 \\ \frac{\partial}{\partial t} (C T) + \nabla \cdot \mathbf{q} = Q \end{cases} \quad \begin{matrix} (1a) \\ (1b) \end{matrix}$$

where $t \in [0, \tau]$ and $\mathbf{x} \in \Omega \subset \mathbb{R}^d$. $T(\mathbf{x}, t)$ may be interpreted as a temperature field, \mathbf{x} denotes the position vector in an open bounded region Ω with a piecewise smooth boundary $\partial\Omega$, t represents time, D is the isotropic thermal conductivity, C is the volumetric specific heat and Q denotes a source term. The total flux \mathbf{q} is the sum of the diffusive and advective fluxes:

$$\mathbf{q} = \mathbf{q}_d + \mathbf{q}_a \quad (2a)$$

$$\mathbf{q}_a = C T \mathbf{u} \quad (2b)$$

where \mathbf{u} is the advection velocity. Equations (1a) and (1b) are addressed as the *constitutive* and the *conservation* equations, respectively. The *fundamental* equation is obtained by substituting (1a) into (1b), yielding:

$$\frac{\partial}{\partial t} (C T) - \nabla \cdot (D \nabla T) + \nabla \cdot (C T \mathbf{u}) = Q \quad (3)$$

System (1) is complemented with initial conditions (4a), Dirichlet boundary conditions (4b), flux boundary conditions (4c) or periodic boundary conditions along x (4d):

$$\begin{cases} T(\mathbf{x}, 0) = f(\mathbf{x}) & \mathbf{x} \in \Omega \end{cases} \quad (4a)$$

$$\begin{cases} T(\mathbf{x}, t) = g(\mathbf{x}, t) & \mathbf{x} \in \partial\Omega_g; t \in [0, \tau] \end{cases} \quad (4b)$$

$$\begin{cases} [\mathbf{q}_d \cdot \mathbf{n}](\mathbf{x}, t) = h(\mathbf{x}, t) & \mathbf{x} \in \partial\Omega_h; t \in [0, \tau] \end{cases} \quad (4c)$$

$$\begin{cases} T(\mathbf{x} + \lambda \mathbf{e}_1, t) = T(\mathbf{x}, t) & \forall \mathbf{x}; t \in [0, \tau] \end{cases} \quad (4d)$$

where \mathbf{e}_1 is the unit vector parallel to the x axis and λ denotes the spatial period, \mathbf{n} is the outwarding unit normal to the boundary $\partial\Omega_h$.

2.2. Weak formulation

For a given triangulation \mathcal{T}_h of $\bar{\Omega}$ [38, ch. 3.1] and a given subdivision of each element into control volumes, a control volume $V \subseteq \Omega$ is considered and the volume indicator distribution is defined as:

$$\phi_V(\mathbf{x}) = \begin{cases} 1 & \text{if } \mathbf{x} \in V \\ 0 & \text{otherwise} \end{cases} \quad (5)$$

The vector equation (1a) is contracted with the vectors $\Phi_x \equiv (\phi_V, 0)$ and $\Phi_y \equiv (0, \phi_V)$ (for $d = 2$) and integrated over the whole space Ω , yielding:

$$\int_{\Omega} D^{-1} \mathbf{q}_d \cdot \Phi_x \, d\mathbf{x} + \int_{\Omega} \nabla T \cdot \Phi_x \, d\mathbf{x} = 0 \quad (6a)$$

$$\int_{\Omega} D^{-1} \mathbf{q}_d \cdot \Phi_y \, d\mathbf{x} + \int_{\Omega} \nabla T \cdot \Phi_y \, d\mathbf{x} = 0 \quad (6b)$$

Using the definition of ϕ_V , the system (6) can be recast in vector form as

$$\int_V D^{-1} \mathbf{q}_d \, d\mathbf{x} + \int_{\partial V} T^- \mathbf{n} \, ds = \mathbf{0} \quad (7)$$

where the integrals act component-wise on the integrand vectors. Here $\mathbf{n} \equiv (n_x, n_y)$ denotes the outward-pointing normal unit vector to $\partial\Omega$. In equation (7) T^- denotes the trace on ∂V of the restriction of the function T to the volume V . The function T must satisfy some regularity conditions in order to apply the divergence theorem to the right-most integrals in (6a) and (6b). Martinez [33] uses the properties of the Dirac's delta distribution to convert the volume integrals in (6a) and (6b) into the surface integral, appearing in (7). A different approach is followed here, based on the theory of *mollifiers* [40]. Let T be a function in $\mathbb{H}^1(V)$ and consider the second integral in (6a). A family of mollifiers $\rho_\epsilon \in \mathcal{C}_0^\infty(\mathbb{R}^2)$, $\epsilon > 0$ is defined as follows

$$\rho_\epsilon(x) = \begin{cases} \frac{1}{\epsilon^2} e^{-\frac{1}{1-|\frac{x}{\epsilon}|^2}} & \text{for } |x| < \epsilon \\ 0 & \text{for } |x| \geq \epsilon \end{cases} \quad (8)$$

A sequence of smooth functions T_ϵ is defined using the convolution [40, ch. 7.2]

$$T_\epsilon(x) = \int_{\mathbb{R}^2} \rho_\epsilon(x - y) E(T(y)) \, dy$$

where $E(\cdot)$ is a linear *extension* operator,

$$E : \mathbb{H}^1(V) \longrightarrow \mathbb{H}^1(\mathbb{R}^2) \quad (9)$$

whose existence can be proved (see, for instance, Salsa [40], ch. 7.8, th. 7.9). It can also be proved [40, ch. 7.8, th. 7.10] that T_ϵ converges to T as $\epsilon \longrightarrow 0$, that is

$$\lim_{\epsilon \longrightarrow 0} \|T - T_\epsilon\|_{\mathbb{H}^1(V)} = 0 \quad (10)$$

The second integral in (6a) can be rearranged as follows:

$$\int_{\Omega} \nabla T \cdot \Phi_x \, d\mathbf{x} = \int_V \frac{\partial T}{\partial x} \, d\mathbf{x} = \lim_{\epsilon \rightarrow 0} \int_V \frac{\partial T_\epsilon}{\partial x} \, d\mathbf{x} \quad (11)$$

The last equality in (11) is a consequence of (10). Namely, using the Cauchy-Schwartz inequality for the scalar product yields:

$$\begin{aligned} \int_V \left(\frac{\partial T_\epsilon}{\partial x} - \frac{\partial T}{\partial x} \right) d\mathbf{x} &\leq |V|^{1/2} \left\| \frac{\partial T_\epsilon}{\partial x} - \frac{\partial T}{\partial x} \right\|_{\mathbb{L}^2(V)} \\ &\leq |V|^{1/2} \|T_\epsilon - T\|_{\mathbb{H}^1(V)} \end{aligned} \quad (12)$$

where the last inequality is due to the fact that, in general, $\|\cdot\|_{\mathbb{L}^2(V)} \leq \|\cdot\|_{\mathbb{H}^1(V)}$. The last equality in (11) follows immediately from (10,12).

Exploiting the smoothness of T_ϵ , the divergence theorem can be applied to the last integral in (11), yielding:

$$\int_V \frac{\partial T_\epsilon}{\partial x} \, d\mathbf{x} = \int_{\partial V} T_\epsilon n_x \, ds \quad (13)$$

Letting now $\epsilon \rightarrow 0$ yields

$$\lim_{\epsilon \rightarrow 0} \int_{\partial V} T_\epsilon n_x \, ds = \int_{\partial V} T^- n_x \, ds \quad (14)$$

thus obtaining the first component of equation (7), again using the convergence of T_ϵ .

Choosing $\mathbf{q} \in \mathbb{H}^1(V; \mathbb{R}^2)$, the weak form of the conservation equation (1b) is obtained by multiplying by a volume indicator distribution ϕ_U , which in principle can be different from ϕ_V and integrating over Ω :

$$\int_{\Omega} \frac{\partial}{\partial t} (C T) \phi_U \, d\mathbf{x} + \int_{\Omega} (\nabla \cdot \mathbf{q}) \phi_U \, d\mathbf{x} = \int_{\Omega} Q \phi_U \, d\mathbf{x} \quad (15)$$

Using the definitions (2) and (5) and the approximation procedure outlined above, equation (15) can be recast as:

$$\int_U \frac{\partial}{\partial t} (C T) \, d\mathbf{x} + \int_{\partial U} C T^- \mathbf{u} \cdot \mathbf{n} \, ds + \int_{\partial U} \mathbf{q}_d^- \cdot \mathbf{n} \, ds = \int_U Q \, d\mathbf{x} \quad (16)$$

Choosing $T, \mathbf{q} \in \mathbb{H}^1(V)$ guarantees the existence of the integrals on V . In addition, a trace theorem asserts that a function in $\mathbb{H}^1(V)$ has a $\mathbb{L}^2(\partial V)$ trace [38, th. 1.3.1 ch. 1], assuring the existence of the boundary integrals appearing in the weak formulation. It is worth mentioning that $T, \mathbf{q} \in \mathbb{H}^1(V)$ does not imply any continuity constraint between *elements*. In addition when $d = 1$ [38, th. 1.3.4 ch. 1]:

$$T, q \in \mathbb{H}^1(V) \Rightarrow T, q \in C^0(\bar{V}),$$

while for $d = 2, 3$, T, \mathbf{q} can be discontinuous in V .

The numerical approximation of (7) and (16) must consider two different configurations for a control volume, according its intersection with the element's boundary being empty or not. As an example, consider a control volume $V \subset \Omega \subset \mathbb{R}^2$ situated at the corner of an element and the second integral in (7). Two edges of the control volume lie in the interior of the element (say e_1 and e_2) and two edges on its boundary (e_3 and e_4). Introducing *numerical traces*, as happens in the DGFEM formulation [14], yields:

$$\int_{\partial V} T^- \mathbf{n} \, ds = \int_{e_1 \cup e_2} T \mathbf{n} \, ds + \int_{e_3 \cup e_4} \hat{T} \mathbf{n} \, ds \quad (17)$$

where \hat{T} is a suitably-defined numerical trace. The definition of numerical traces is crucial, since it affects the consistency, stability and accuracy of the resulting discontinuous method [14].

It is worth comparing the *mixed*, weak formulation (7) and (16) with the weak formulation of the *fundamental* equation (3). The latter can be obtained by *weighting* the residual of equation (3) with the volume indicator distribution ϕ_V and integrating over Ω , obtaining:

$$\int_V \frac{\partial}{\partial t} (C T) \, d\mathbf{x} + \int_{\partial V} [C T^- \mathbf{u} - D \nabla T^-] \cdot \mathbf{n} \, ds = \int_V Q \, d\mathbf{x} \quad (18)$$

The integrals appearing in (18) exist if $C, D, \mathbf{u} \in \mathbb{H}^1(V)$ and $T \in \mathbb{H}^2(V)$, because in this formulation the trace of ∇T must lie in $\mathbb{L}^2(\partial V)$, implying $\nabla T \in \mathbb{H}^1(V)$. Therefore, for the scalar field T and for the other terms appearing in equation (18) higher regularity is required, compared to the mixed formulation.

3. Numerical approximation

3.1. Domain discretization

The domain Ω is subdivided by a tessellation of elements. In the present work, only one-dimensional and two-dimensional, quadrilateral elements are considered. Each element Ω^e is partitioned into *control volumes* V . Differently from continuous CVFEM methods, each control volume is entirely contained in a single element. A coordinate transformation is used to map the physical element Ω^e into the canonical element $\hat{\Omega} \equiv [-1, 1]^d$, where d denotes the dimension of Ω ($d = 1$ or 2 in this work). In general, the mapping is based on an independent set of interpolatory piecewise-polynomials \hat{N}_j , which respect inter-element continuity:

$$\mathbf{x}^e(\boldsymbol{\xi}) = \sum_{j=1}^{N^e} \hat{N}_j(\boldsymbol{\xi}) \mathbf{x}_j^e \quad (19)$$

where $\{\mathbf{x}_j^e\}_{j=1}^{N^e}$ are the physical coordinates of the N^e element's geometrical nodes and $\boldsymbol{\xi} \in \hat{\Omega}$ is the coordinate in the transformed space. In the proposed formulation the control volume's edges in the one-dimensional, transformed element $\hat{\Omega}$ lie either on $P^e + 2$ Gauss-Lobatto-Legendre quadrature nodes or on $-1, +1$ and on P^e Gauss-Legendre quadrature nodes. The two-dimensional, quadrilateral element is easily obtained by tensor-product of the one-dimensional element in transformed space.

3.2. Finite dimensional subspace and basis functions

The unknowns $T(\mathbf{x}, t)$ and $\mathbf{q}(\mathbf{x}, t)$ are approximated by element-based polynomial expansions [26]. Approximations $T_h(\cdot, t)$ and $\mathbf{q}_h(\cdot, t)$ are chosen in the same finite-dimensional subspace of $\mathbb{H}^1(\Omega)$ [38], spanned by a basis of interpolatory piecewise polynomials $N_j(\boldsymbol{\xi})$, defined in the transformed space, which do not respect inter-element continuity. For example, the restriction T_h^e of T_h to the element Ω^e is given by

$$T_h^e(\boldsymbol{\xi}) \equiv \sum_{i=1}^{P^e+1} N_i(\boldsymbol{\xi}) T_i^e \quad (20)$$

where $\{T_i^e\}_{i=1}^{P^e+1}$ are the nodal values of T_h in the element Ω^e . In principle, the interpolation nodes may be located everywhere inside an element. Nevertheless, Gauss-Legendre or Gauss-Lobatto-Legendre quadrature nodes result

in general in well-conditioned systems of equations [20, 24, 33] and are used in the present study.

The finite-element approximation of one-dimensional problems often exhibits the property known as *superconvergence* on some special points [56, ch.14], that is, if a quantity is sampled on those points the error decreases more rapidly than elsewhere within the element. In the proposed mixed formulation, it is verified that the diffusion flux \mathbf{q}_d exhibits superconvergence when sampled at the P^e Gauss quadrature points within each element. In general, mixed finite-element methods do not require the interpolation of the *flux* variable onto the superconvergence points, as the flux at the interpolation nodes has the same order of accuracy as the transported quantity [56, ch.11]. Numerical experiments reveal that the proposed methodology, endowed with the LDG formulation of the numerical trace [2], though based on the mixed formulation, requires interpolation of the flux variable onto the superconvergence points, in order to achieve the same order of accuracy of the scalar unknown. This feature is confirmed by Fourier analysis. Preliminary results, not reported in this work, show that different formulations of the numerical trace allow to achieve $P^e + 1$ accuracy for \mathbf{q}_d at the interpolation nodes.

3.3. Approximation of the weak formulation

As this preliminary work focuses mainly on spatial-discretization, a simple yet robust implicit-Euler scheme for the time-discretization is used to present the main features of the method. The resulting system of linear algebraic equations is

$$\begin{bmatrix} \mathbf{M}^{(q)} & \mathbf{L} \\ \Delta t \mathbf{F} & \mathbf{M}^{(T)} + \Delta t \mathbf{A} \end{bmatrix} \begin{Bmatrix} \mathbf{q}^{n+1} \\ \mathbf{T}^{n+1} \end{Bmatrix} = \begin{Bmatrix} \mathbf{0} \\ \mathbf{r} \end{Bmatrix} \quad (21)$$

For the one-dimensional case, the components of the coefficient matrix and of the right-hand side are obtained by using the approximations (19) and (20) and by approximating the integrals appearing in equations (7) and (16) using the Gauss-Legendre quadrature:

$$M_{ij}^{(q)} = \int_{V_i} D^{-1} N_j dx \quad (22a) \quad L_{ij} = \sum_{f_k} [N_j n]_{f_k} \quad (22b)$$

$$A_{ij} = \sum_{f_k} [C N_j u n]_{f_k} \quad (22c) \quad F_{ij} = \sum_{f_k} [N_j n]_{f_k} \quad (22d)$$

$$M_{ij}^{(T)} = \int_{V_i} C N_j dx \quad (22e) \quad r_i = \Delta t \int_{V_i} Q dx - \sum_j M_{ij}^{(T)} T_j^n \quad (22f)$$

where, in the one-dimensional case, the unit normal vector is $n = \pm 1$. The vectors $\mathbf{T} = \{T_j\}$ and $\mathbf{q} = \{q_j\}$ contain the unknown nodal values of T_h and \mathbf{q}_h . The actual and previous time steps are denoted by the superscripts $n+1$ and n , respectively. The index f_k is used to address the *faces* (end-points, in 1D) of a control volume.

3.4. Inter-element coupling and boundary conditions

As for DGFEM, the approximate solution (T_h, \mathbf{q}_h) of DCVFEM does not have to satisfy any inter-element continuity constraint [14]. As a consequence, the method is prone to be highly parallelizable when fully-explicit time-stepping schemes are used, as is customary in purely-hyperbolic problems. In addition, the method can easily handle different types of approximations in different elements (p -adaptivity) [26]. As the present work focuses on the diffusion operator, implicit time-stepping schemes are also considered, due to the severe stability limits imposed by explicit methods. In this case, the inter-element coupling provided by the numerical fluxes prevents a straightforward parallelization and, in addition, the coefficient matrix is no more block-diagonal, though still very sparse, as is evident in figure 1(a), for the an unsteady diffusion problem using 10 elements with $P^e = 3$. Figure 1(a) shows the structure of the matrix without reordering, while the pattern depicted by figure 1(b) results from application of a reverse Cuthill-McKee ordering algorithm [27].

On the element's boundary, *numerical fluxes* \widehat{T}_h and $\widehat{\mathbf{q}}_h$ have to be defined in order to stabilize the discontinuous method [14, 26]. The LDG formulation of the diffusion numerical fluxes is used [13], where inside the domain it is assumed:

$$\begin{aligned} \widehat{T}_h &= \{T_h\} \\ \widehat{\mathbf{q}}_h &= \{\mathbf{q}_h\} + C_{11} \llbracket T_h \rrbracket \end{aligned} \quad (23)$$

with the operators $\{\cdot\}$ and $\llbracket \cdot \rrbracket$, denoting the inter-element average and jump, defined as:

$$\begin{aligned} \{T_h\} &\equiv \frac{1}{2} (T_h^- + T_h^+) & \{\mathbf{q}_h\} &\equiv \frac{1}{2} (\mathbf{q}_h^- + \mathbf{q}_h^+) \\ \llbracket T_h \rrbracket &\equiv (T_h^- \mathbf{n}^- + T_h^+ \mathbf{n}^+) & \llbracket \mathbf{q}_h \rrbracket &\equiv (\mathbf{q}_h^- \cdot \mathbf{n}^- + \mathbf{q}_h^+ \cdot \mathbf{n}^+) \end{aligned} \quad (24)$$

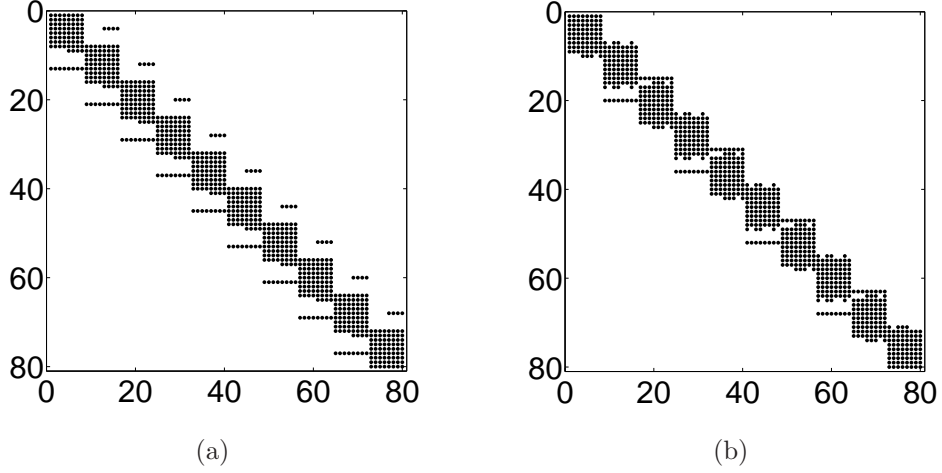


Figure 1: Sparsity of the coefficient matrix for the solution of an unsteady diffusion problem using 10 elements with $P^e = 3$ (a) before reordering and (b) after application of a reverse Cuthill-McKee ordering algorithm [27].

On the domain's boundary $\partial\Omega$, the following distinct formulations apply:

Dirichlet boundary $\partial\Omega_g$. According to Cockburn [14]:

$$\begin{aligned}\widehat{T}_h &= g(\mathbf{x}, t) \\ \widehat{\mathbf{q}}_h &= \mathbf{q}_h - C_{11} \llbracket T_h \rrbracket\end{aligned}\tag{25}$$

Flux boundary $\partial\Omega_h$. According to Li [26]:

$$\begin{aligned}\widehat{T}_h &= T_h(\partial\Omega, t) \\ \widehat{\mathbf{q}}_h \cdot \mathbf{n} &= h(\mathbf{x}, t)\end{aligned}\tag{26}$$

Periodic boundary. As information is exchanged between neighboring elements only through numerical fluxes, periodic boundary conditions are enforced by matching the corresponding periodic boundaries.

Arnold et al. [2] prove that, in order to achieve a stable LDG-DGFEM formulation, the coefficient C_{11} must be positive, of order h^{-1} , where h the element's size and proportional to the polynomial order of the element. In this work it is assumed:

$$C_{11} = \frac{\alpha P^e D}{h}\tag{27}$$

with $\alpha > 0$. The results of the Fourier analysis, reported in section 4, confirm that this choice yields a stable semi-discrete DCVFEM for unsteady diffusion-type problems.

The present work is aimed to develop a general framework for the solution of diffusion and advection-diffusion problems by the DCVFEM method. Therefore, a formulation of numerical fluxes is sought which, though possibly non-optimal in terms of accuracy and stability, yields stable solutions which are convergent both upon h - and p - refinement, and is general enough to accommodate different formulations of numerical fluxes with minor modifications.

The simplest central flux formulation,

$$\begin{aligned}\widehat{\mathbf{q}}_h &= \frac{1}{2} (\mathbf{q}_h^- + \mathbf{q}_h^+) \\ \widehat{T}_h &= \frac{1}{2} (T_h^- + T_h^+)\end{aligned}\tag{28}$$

was applied originally by Bassi and Rebay [6] and later studied by Cockburn and Shu [13], who proved that the resulting DGFEM method converges at a rate $P^{(e)}$, for piecewise polynomials of degree $P^{(e)}$. Application of the central-flux formulation to the proposed DCVFEM yields a singular coefficient matrix for steady-diffusion problems. This can be easily verified for the one-dimensional, stationary diffusion equation with Dirichlet boundary conditions, discretized using linear elements with interpolation nodes on the boundaries of the elements. A uniform mesh with unitary grid spacing is considered. The left-hand side of the algebraic equations, resulting from the DCVFEM discretization for any an element $I^{(j)} = [x_j, x_{j+1}]$, $j = 1 \dots N - 1$, is given by

- Left-most element, $j = 1$:

$$\begin{aligned}q_{j+1}^- - q_j^+ \\ q_{j+1}^+ - q_j^+ \\ \left(\frac{3}{4}q_j^+ + \frac{1}{4}q_{j+1}^-\right) + T_{j+1}^- + T_j^+ \\ \left(\frac{1}{4}q_j^+ + \frac{3}{4}q_{j+1}^-\right) + T_{j+1}^+ - T_j^+\end{aligned}\tag{29a}$$

- Internal element, $1 < j < N - 1$:

$$\begin{aligned}
& q_{j+1}^- - q_j^- \\
& q_{j+1}^+ - q_j^+ \\
& \left(\frac{3}{4}q_j^+ + \frac{1}{4}q_{j+1}^- \right) + T_{j+1}^- - T_j^- \\
& \left(\frac{1}{4}q_j^+ + \frac{3}{4}q_{j+1}^- \right) + T_{j+1}^+ - T_j^+
\end{aligned} \tag{29b}$$

- Right-most element, $j = N - 1$:

$$\begin{aligned}
& q_{j+1}^- - q_j^- \\
& q_{j+1}^- - q_j^+ \\
& \left(\frac{3}{4}q_j^+ + \frac{1}{4}q_{j+1}^- \right) + T_{j+1}^- - T_j^- \\
& \left(\frac{1}{4}q_j^+ + \frac{3}{4}q_{j+1}^- \right) - T_{j+1}^- - T_j^+
\end{aligned} \tag{29c}$$

It can be readily verified that the solution vector, assembled from nodal temperatures and fluxes defined as

$$\begin{aligned}
q_j &= 0 & \forall j = 1 \dots N \\
T_j &= (-1)^j \alpha, \alpha \in \mathbb{R} \setminus \{0\} & \forall j = 1 \dots N
\end{aligned} \tag{30}$$

belongs to the kernel of the coefficient matrix, assembled from the equations (29). Therefore, the coefficient matrix is singular. The unphysical solution (30) yields the well-known *checkerboarding* effect [37].

The LDG approach by Cockburn and Shu [13], constructed to deal with the mixed form of the diffusion equation, can be easily incorporated into a more general Discontinuous Galerkin formulation [10], where the numerical flux for the scalar field depends (linearly) on the jump in the flux variable. In DGFEM methods based on the LDG formulation the conservation property at element level is preserved since the numerical fluxes attain a unique value on the inter-element boundaries [2]. Moreover, the possibility to compute the flux \mathbf{q} locally (at element level) as a function of the scalar unknown

T [13] allows a certain flexibility in the choice of the method for solving the resulting algebraic systems. In the DGFEM framework, the order of accuracy for the LDG representation of numerical fluxes is $P^{(e)} + 1$ for a polynomial interpolation of order $P^{(e)}$ [44, 55].

In the present work, the numerical flux associated with advection is defined by the upwind strategy [26]:

$$\tilde{T}_h = T_h^- \max(\mathbf{u} \cdot \mathbf{n}^-, 0) + T_h^+ \max(\mathbf{u} \cdot \mathbf{n}^+, 0) \quad (31)$$

3.5. Conservation issues

As mentioned by Cockburn [14], DGFEM methods are locally conservative on each element, provided that a sum of weighted functions is equal to unity at any point in the element. Commonly used Lagrange and Serendipity shape functions meet this requirement [56, ch.8]. The DCVFEM method is locally conservative on each control volume and, by summation and cancellation of fluxes, on each element, provided that the numerical fluxes are expressed by conservative formulations [8]. In addition, the weak enforcement of Dirichlet boundary conditions maintains the global conservation property, which is not the case with the traditional strong enforcement in continuous CVFEMs [33].

4. Fourier analysis

The Fourier analysis [1, 55] is used to investigate the stability, accuracy and resolution properties of the proposed method and to provide additional insight into particular features, pointed out by the results of the numerical simulations.

4.1. Unsteady diffusion

The unsteady, one-dimensional diffusion problem with periodic boundary conditions is described by the following set of non-dimensional equations:

$$\left\{ \begin{array}{l} q^* + \frac{\partial \theta}{\partial x^*} = 0 \end{array} \right. \quad (32a)$$

$$\left\{ \begin{array}{l} \frac{\partial \theta}{\partial \text{Fo}_h} + \frac{\partial q^*}{\partial x^*} = 0 \end{array} \right. \quad (32b)$$

$$\left\{ \begin{array}{l} \theta(x^* + N) = \theta(x^*) \end{array} \right. \quad (32c)$$

$$\left\{ \begin{array}{l} \theta(x^*, 0) = e^{i 2 \pi k x^* / N} \end{array} \right. \quad (32d)$$

where the domain, of length L , is subdivided into N equally-sized elements of width h . The dimensionless coordinate is $x^* \equiv x/h$, $N \equiv L/h$ is the dimensionless domain length, the dimensionless time is defined by the cell Fourier number $\text{Fo}_h \equiv Dt/(Ch^2)$, the dimensionless heat flux is $q^* \equiv qh/(DT_0)$ and the dimensionless temperature is $\theta \equiv T/T_0$. The reference temperature T_0 is the amplitude of the initial condition (32d). The dimensionless LDG coefficient C_{11}^* for the LDG numerical flux is given by

$$C_{11}^* = C_{11}h/D = \alpha P^e \quad (33)$$

From now on, the complex exponential e^{ia} will be denoted by the compact notation $W(a)$, where $a \in \mathbb{R}$, the symbol \widehat{k} will denote the dimensionless wavenumber $2\pi k/N$, with $k \in \mathbb{Z}$. The center of each element is denoted by x_e^* , and the edges of the e -th element have coordinates $x_e^* \mp 1/2$. The interpolation nodes, $n_j, j = 1, \dots, N_n$, are equally spaced in the whole domain. The total number of nodes is $N_n = (P^e + 1)N$. The control-volume faces are located as specified in section 3.1. In the present study, the results for polynomial order $P^e = 1$ (linear elements), $P^e = 2$ (parabolic elements), $P^e = 3$ and $P^e = 4$ are presented. The details of the Fourier analysis for $P^e = 1$, the linear case, are reported in A.1.

The analytic solution to problem (32) is

$$\theta^{(an.)}(x^*, \text{Fo}_h) = e^{-\widehat{k}^2 \text{Fo}_h} W(\widehat{k} x^*) \quad (34)$$

The calculated Discrete Fourier Transform (DFT hereafter) of the non-dimensional temperature θ , in the linear case, can be expressed as:

$$\Theta_k = a_1 \mathbf{V}_1 e^{\lambda_1 \text{Fo}_h} + a_2 \mathbf{V}_2 e^{\lambda_2 \text{Fo}_h} \quad (35)$$

where $\lambda_{1,2}$ are the eigenvalues of the amplification matrix \mathbf{G} of the system (32) (see A.1) and they turn out to be purely real. \mathbf{V}_1 and \mathbf{V}_2 are the corresponding eigenvectors. The free coefficients a_1 and a_2 are used to enforce the initial condition (32d). For $P^e = 1$ a Taylor-series expansion of $\lambda_{1,2}$ with respect to \widehat{k} yields:

$$\begin{aligned} \lambda_1 &= -\widehat{k}^2 + \mathcal{O}(\widehat{k}^4) \\ \lambda_2 &= -8C_{11}^* - \widehat{k}^2(3 - C_{11}^*) + \mathcal{O}(\widehat{k}^4) \end{aligned} \quad (36)$$

showing that λ_1 is an approximation of the exact eigenvalue $-\widehat{k}^2$, thus it is to be regarded as the *true* eigenvalue, while λ_2 is a *spurious* eigenvalue. It turns out that only for $\alpha > 0$ in (33) both normalized eigenvalues $\lambda_{1,2}(\widehat{k})/\widehat{k}^2$ are negative, for any value of \widehat{k} , resulting in stable solutions. For $\alpha \leq 0$ the spurious eigenvalue becomes positive and the method is unstable. Therefore, only positive values of C_{11}^* must be used in order to guarantee stability.

For $P^e = 1$ the Taylor expansion of the numerical solution Θ_k with respect to \widehat{k} is compared with the DFT of the analytical solution (34), sampled at the nodal points, showing that the method is second-order accurate (see A.1). The calculated DFT \mathbf{Q}_k of the non-dimensional flux q^* can now be obtained from the constitutive equation (32a). A Taylor series expansion with respect to \widehat{k} compared with the DFT of the analytical flux, sampled at the nodes, shows that the computed flux is first order accurate (see A.1). The element's mid-point is the superconvergence point for a linear element [56, ch.14]. Linear interpolation of the computed flux at this point yields a second-order accurate approximation of the analytical flux at the same point (see A.1). For $P^e = 2, 3$ and 4, it is verified that the orders of accuracy are $P^e + 1$, P^e and $P^e + 1$ for the scalar and the flux at the interpolation nodes and for the flux at the superconvergence nodes, respectively.

4.1.1. Dispersion/diffusion characteristics

Results of the Fourier analysis for the diffusion equation can be conveniently interpreted in terms of dispersion or dissipation errors [32]. Dispersion errors result in waves, corresponding to different wavenumbers, traveling at different velocity. Diffusion errors can be related to the amount of numerical diffusivity, either positive or negative, introduced by a numerical method.

The solution (35) to the discrete problem, for the left node of an element with $P^e = 1$, can be recast as

$$\Theta_k = F(\widehat{k}, \text{Fo}_h, C_{11}^*) \left[e^{-\widehat{k}^2 \text{Fo}_h} W \left(-\frac{\widehat{k}}{4} \right) \right] \quad (37)$$

The term inside square brackets in (37) corresponds to the analytic solution. $F(\widehat{k}, \text{Fo}_h, C_{11}^*)$ is a complex-valued function, in general, so it can be equivalently expressed as

$$F(\widehat{k}, \text{Fo}_h, C_{11}^*) = e^{-(\widehat{k}_e^2 - \widehat{k}^2) \text{Fo}_h} W \left(-\widehat{k} \text{Pe}_h \text{Fo}_h \right) \quad (38)$$

where \widehat{k}_e denotes the dimensionless effective wavenumber, while Pe_h denotes the effective cell-Péclet number [32]

$$\text{Pe}_h = \frac{h c_e}{D} \quad (39)$$

with c_e being the *numerical* advection velocity. As c_e depends on \widehat{k} , each Fourier mode travels with different velocity. The effective wavenumber \widehat{k}_e quantifies the intensity of numerical dissipation: $\widehat{k}_e > \widehat{k}$ implies that the computed solution is subject to a more intense damping than the analytic solution, so the method is *overdiffusive*. The effective Péclet number Pe_h quantifies the relative intensity of the dispersive error, as can be inferred by recasting Pe_h as follows

$$\text{Pe}_h = \frac{h^2/D}{h/c_e} \equiv \frac{\tau_d}{\tau_a} \quad (40)$$

where τ_d and τ_a denote the time-scale associated with real diffusion and numerical advection, respectively. The larger these time-scales, the weaker the associated transport phenomena. Therefore, $\text{Pe}_h \gg 1$ means that the numerical advection is considerably more effective than the real diffusion in transporting the scalar T . In the analytic solution, $\text{Pe}_h = 0$.

Figure 2 shows the effective wavenumber \widehat{k}_e as a function of \widehat{k} , for different values of the coefficient α in (33) and for the element's leftmost nodes. The results on the other nodes, not reported for brevity, are quite similar, implying that the dissipation error is almost constant with position inside the element. Results obtained by a second-order and a fourth-order, central finite-difference schemes (FD2 and FD4 hereafter) and by a linear and a parabolic GFEM schemes (GFEM1 and GFEM2 hereafter) are also reported for comparison. The modified wavenumbers for FD2, FD4 and GFEM1 can be calculated analytically:

$$\widehat{k}_e = \sqrt{2[1 - \cos(\widehat{k})]} \quad \text{FD2} \quad (41)$$

$$\widehat{k}_e = \sqrt{\frac{1}{6} \cos(2\widehat{k}) - \frac{8}{3} \cos(\widehat{k}) + \frac{5}{2}} \quad \text{FD4} \quad (42)$$

$$\widehat{k}_e = \sqrt{6 \frac{1 - \cos \widehat{k}}{2 + \cos \widehat{k}}} \quad \text{GFEM1} \quad (43)$$

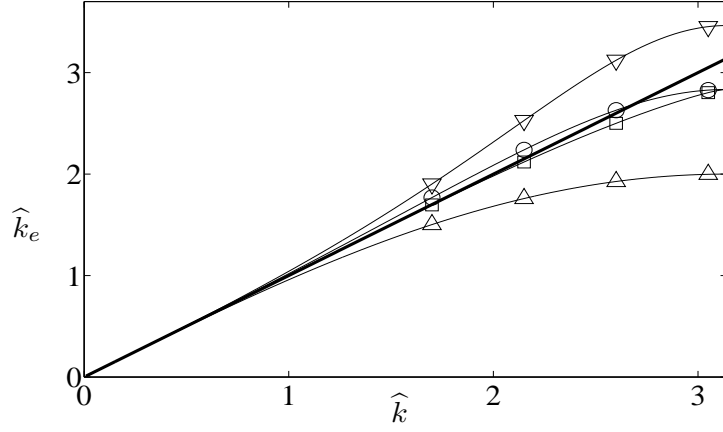
The expression of \widehat{k}_e for the GFEM2 method is obtained numerically. The following considerations can be drawn:

- The effective wavenumber depends very weakly on Fo_h .
- In DGFEM, the coefficient C_{11}^* is related to the intensity of numerical dissipation [14]. This is confirmed also for the proposed DCVFEM: for all considered values of P^e , increasing α from 0.1 to 10 in (33) yields an increase of \widehat{k}_e . Compared to the other considered methods, DCVFEM with $\alpha = 10$ yields very weak numerical dissipation, concentrated in the highest-wavenumber range.
- In the cases $P^e = 1$ and $P^e = 2$, for all considered values of C_{11}^* the DCVFEM method provides a sensibly smaller amount of artificial dissipation (either positive or negative) than the other considered methods, which are under-diffusive (central finite difference) or overdiffusive (GFEM) across the entire wavenumber range.
- For $P^e = 2$ and $P^e = 4$ and $\alpha = 0.1$, DCVFEM exhibits a larger dissipation error in the high wavenumber range compared to the respective lower even-ordered accuracy cases, namely $P^e = 1$ and $P^e = 3$, respectively. This feature is not confirmed with $\alpha = 10$, showing the sensitivity of the proposed formulation on the C_{11} coefficient.

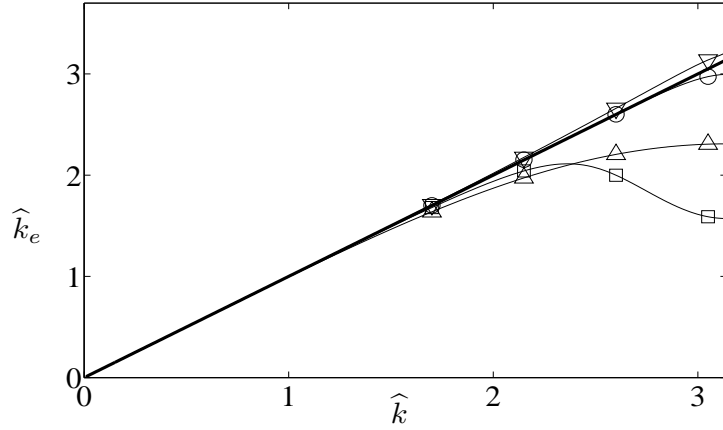
Figures 3 and 4 show the effective cell-Péclet number Pe_h as a function of \widehat{k} , for $P^e = 1, 2$ and for $P^e = 3, 4$, respectively. Reported results are obtained with different values of the coefficient α in (33) and at $\text{Fo}_h = 1$. Pe_h vanishes rapidly at larger times Fo_h and for $\text{Fo}_h = 10$ (not shown for brevity) it is negligibly small. Central finite difference and GFEM schemes are free from dispersion errors in the solution of the diffusion equation. From the reported results, the following considerations can be drawn:

- The dispersion error affects more severely the high-wavenumber range.
- The value of C_{11}^* affects the distribution of Pe_h over the entire range of wavenumbers. The value of α yielding the smallest dispersion error depends on the polynomial order P^e and on the considered range of wavenumbers: choosing $\alpha = 10$ yields the lowest overall dispersion error for all considered values of P^e .
- In the high-wavenumber range, the dispersion error is larger for schemes of even order P^e than for schemes with odd order $P^e - 1$.

- Figure 3 shows results for the element's leftmost node. The results for the rightmost node, not shown here for brevity, have the same magnitude but opposite sign. This implies that the numerical solution is squeezed or stretched between left and right nodes, with an alternating pattern in space. This behavior is confirmed by the fact that in the

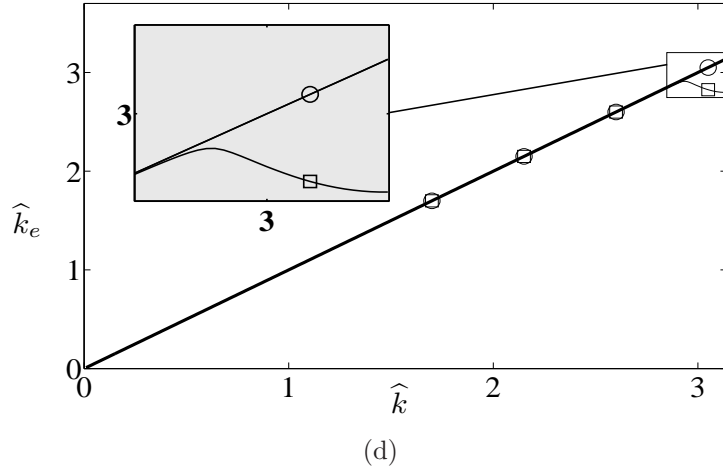
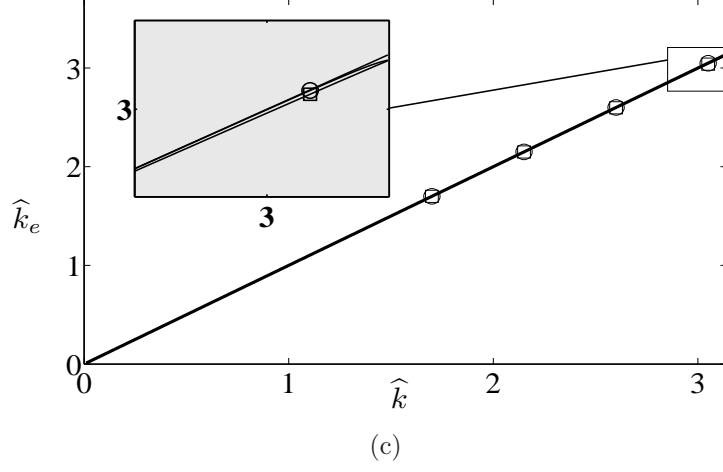


(a)



(b)

Figure 2: Distribution of the effective wavenumber \hat{k}_e with respect to the dimensionless wavenumber \hat{k} , for (a) $P^e = 1$, (b) $P^e = 2$, (c) $P^e = 3$ and (d) $P^e = 4$. Symbol \square : DCVFEM with $\alpha = 0.1$; symbol \circ : DCVFEM with $\alpha = 10$; thick solid line: exact solution; symbol \triangle : (a) FD2 and (b) FD4; symbol ∇ : (a) GFEM1 and (b) GFEM2.



case $P^e = 2$ the results for the central node, not reported for brevity, show no dispersion error, that is, $\text{Pe}_h = 0$ for all wavenumber range. Figure 4 shows results for higher orders $P^e = 3, 4$, for element's (a) outer-leftmost and (b) inner-leftmost nodes. Results for corresponding rightmost nodes have same magnitude but opposite sign and are not shown for brevity. Numerical dispersion has significantly lower magnitude compared to lower orders $P^e = 1, 2$. As a confirmation to what observed for the lower orders $P^e = 1, 2$, the numerical solution is squeezed or stretched from outer to inner nodes, indeed the entity

of dispersion decreases from the outer, figure 4(a), to the inner node, figure 4(b), and, in the case $P^e = 4$ the central node (not reported for brevity) is free from dispersion error.

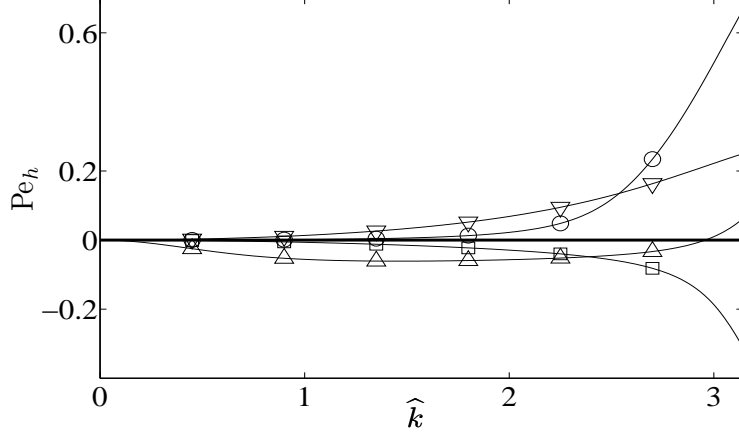


Figure 3: Distribution of the cell-Péclet number Pe_h with respect to the dimensionless wavenumber \hat{k} , at time $Fo_h = 1$ for $P^e = 1, 2$. Symbol \triangle : $\alpha = 0.1$, $P^e = 1$; symbol ∇ : $\alpha = 10$, $P^e = 1$; symbol \circ : $\alpha = 0.1$, $P^e = 2$; symbol \square : $\alpha = 10$, $P^e = 2$.

4.2. Unsteady advection

In the purely advective case the non-dimensional form of the conservation equation (1b) is:

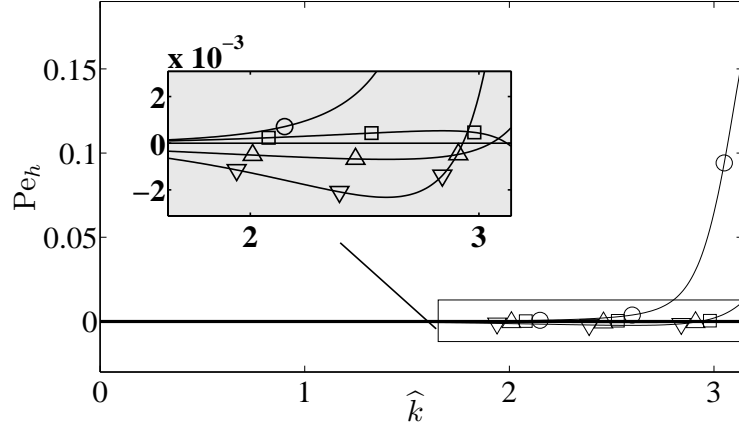
$$\frac{\partial \theta}{\partial C^*} + \frac{\partial \theta}{\partial x^*} = 0 \quad (44)$$

coupled with periodic boundary conditions (32c) and initial condition (32d). $C^* \equiv u t/h$ is the CFL number [1, p.162], with u the advection velocity. The CFL number can be interpreted both as the non-dimensional time and as the non-dimensional true advection velocity. The analytic solution is

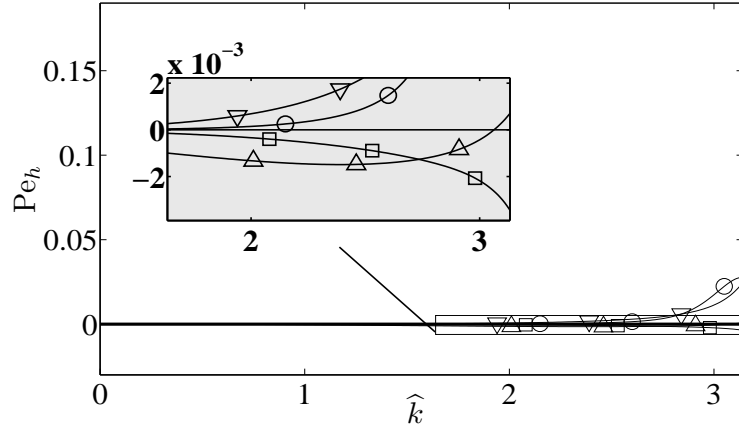
$$\theta^{(an.)}(x^*, C^*) = W \left(\hat{k} (x^* - C^*) \right) \quad (45)$$

For $P^e = 1$, the numerical trace is defined by the upwind strategy (31). The calculated Fourier modes can be expressed as

$$\Theta_k = a_1 \mathbf{V}_1 e^{\lambda_1 C^*} + a_2 \mathbf{V}_2 e^{\lambda_2 C^*} \quad (46)$$



(a)



(b)

Figure 4: Distribution of the cell-Péclet number Pe_h with respect to the dimensionless wavenumber \hat{k} , at time $Fo_h = 1$ for $P^e = 3, 4$. Symbol \triangle : $\alpha = 0.1$, $P^e = 3$; symbol ∇ : $\alpha = 10$, $P^e = 3$; symbol \circ : $\alpha = 0.1$, $P^e = 4$; symbol \square : $\alpha = 10$, $P^e = 4$. (a) element's left outer node, (b) element's left inner node.

where $\lambda_{1,2}$ are the eigenvalues of the amplification matrix \mathbf{G} (see A.2) and $\mathbf{V}_{1,2}$ are the corresponding eigenvectors. The coefficients a_1 and a_2 are calculated from the initial condition (32d). The eigenvalues $\lambda_{1,2}$ of the amplification matrix are both complex numbers, in this case. The Taylor expansion

of the imaginary part with respect to \widehat{k} yields:

$$\begin{aligned}\lambda_1 &= -i\widehat{k} + O(\widehat{k}^2) \\ \lambda_2 &= 2i\widehat{k} - 4 + O(\widehat{k}^2)\end{aligned}\tag{47}$$

showing that λ_1 is an approximation of the *true* eigenvalue, while λ_2 is the *spurious* eigenvalue. The real parts of the eigenvalues, not shown for brevity, are negative throughout the entire wavenumber range, with $\text{Re}(-\widehat{\lambda}_2) \gg \text{Re}(-\widehat{\lambda}_1)$ and $\text{Re}(\widehat{\lambda}_2) \rightarrow -4$ as $\widehat{k} \rightarrow 0$. This suggests an overall stable and dissipative behavior of the method, with the spurious component of the solution decaying much faster than the *true* component with time. The Taylor-series expansion of the numerical solution with respect to \widehat{k} yields a second-order accurate approximation of $\Theta_k^{(\text{an.})}$, that is, the DFT of the analytic solution (45) sampled at the nodes. Analogous results for the cases $P^e = 2, 3$ and 4 show that the method is $P^e + 1$ accurate.

4.2.1. Dispersion/diffusion characteristics

The solution (46) for the left node of an element can be recast as

$$\Theta_k(\widehat{k}, C^*) = F(\widehat{k}, C^*) \left[W \left(-\widehat{k} \left(\frac{1}{4} + C^* \right) \right) \right]\tag{48}$$

The term inside square brackets in (48) is the analytic solution. In general, $F(\widehat{k}, C^*)$ is a complex-valued function, and can be equivalently expressed as

$$F(\widehat{k}, C^*) = \exp \left(-\frac{\widehat{k}^2 C^*}{\text{Pe}_h^{(\text{num.})}} \right) W \left(-\widehat{k} (C_e^* - C^*) \right)\tag{49}$$

where the non dimensional coefficient $\text{Pe}_h^{(\text{num.})}$ represents the numerical cell-Péclet number and C_e^* the *effective* (numerical) CFL number. A physical interpretation of $1/\text{Pe}_h^{(\text{num.})}$ and C_e^* is:

- $1/\text{Pe}_h^{(\text{num.})}$ represents the numerical diffusivity of the scheme. Positive values of $1/\text{Pe}_h^{(\text{num.})}$ indicate that the calculated solution is damped by numerical diffusion.
- C_e^* gives information about the effective dispersion of the scheme. In fact in the analytic solution $C_e^* = C^*$, therefore the ratio C_e^*/C^* provides a measure of the dispersion error.

Figure 5 reports the plot of $1/\text{Pe}_h^{(\text{num.})}$ versus the wavenumber \hat{k} , at different values of C^* , for $P^e = 1, 2, 3, 4$. It can be concluded that:

- Due to the non symmetric nature of the advection problem, results for each node of the element are different, but the scheme is in general diffusive ($1/\text{Pe}_h^{(\text{num.})} > 0$) in the high-wavenumber range. The right (i.e. downstream w.r.t. the direction of the wind) nodes show a greater amount of numerical diffusivity.
- The amount of numerical diffusivity decreases significantly as the schemes' order is increased.
- As C^* increases, the method becomes progressively more diffusive (or less counter-diffusive) in the entire wavenumber range.
- The scheme tends to become non-diffusive in the low-wavenumber range as C^* increases.

Figure 6 shows the dependence on \hat{k} of the ratio C_e^*/C^* , for different values of C^* at each element's node, for $P^e = 1, 2, 3, 4$. The following conclusions can be drawn:

- The scheme is in general more dispersive in the high-wavenumber range.
- The dispersion error is significantly reduced as the polynomial order increases.
- At low values of dimensionless time C^* the dispersion error shows different trends on different nodes, yet it becomes similar on all element's nodes as C^* increases.

Van den Abeele et al. [46] use Fourier analysis to investigate the characteristics of the Spectral Volume Method (SVM) for the one-dimensional conservation law. It is recognized that the upwind SVM with Gauss-Lobatto distribution of the control-volume boundaries is weakly unstable when the third-order TVD Runge-Kutta scheme [43] is used for time integration, with a CFL number equal to 0.125. As the present work focuses on diffusion-dominated problems, only implicit schemes are used for time-integration, so that no instability has been detected in the considered test-cases. The

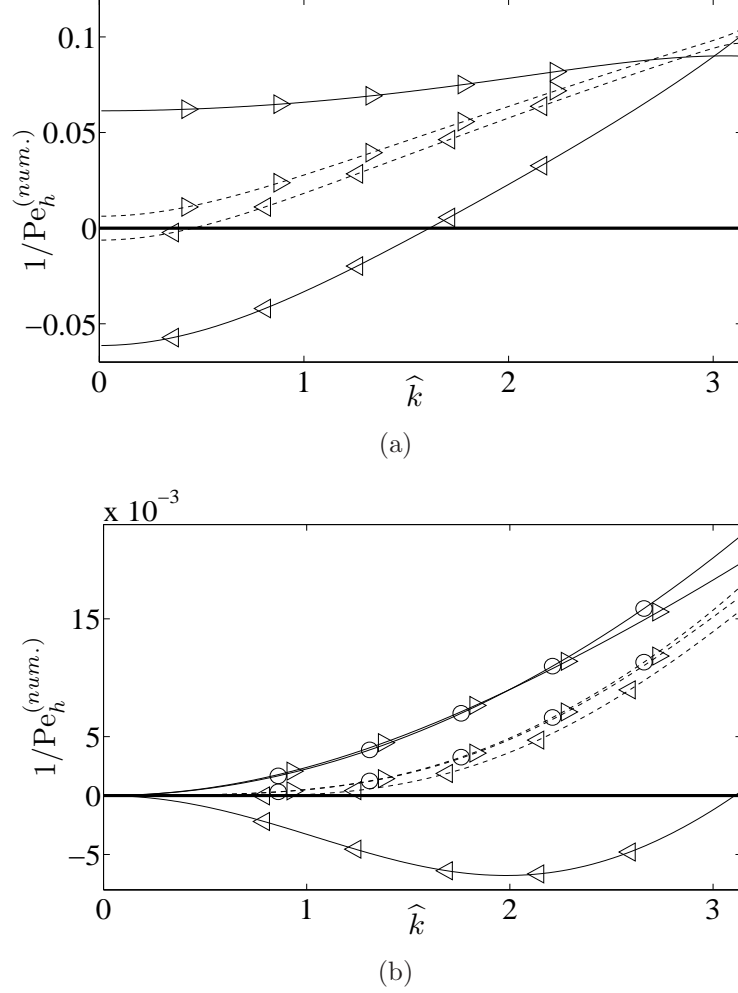
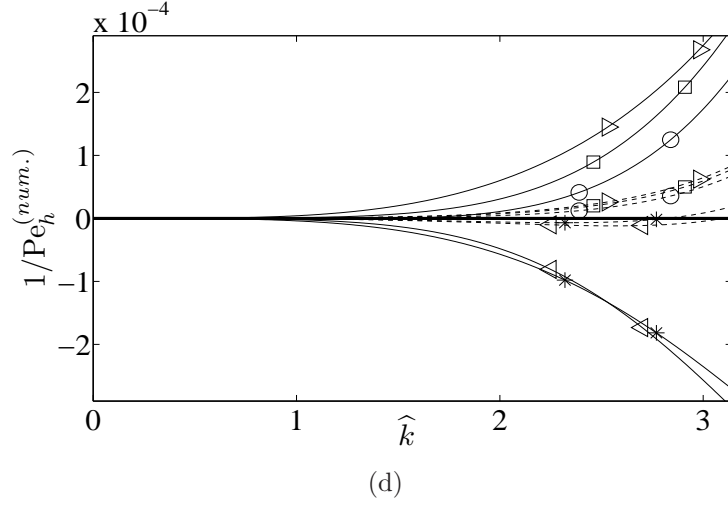
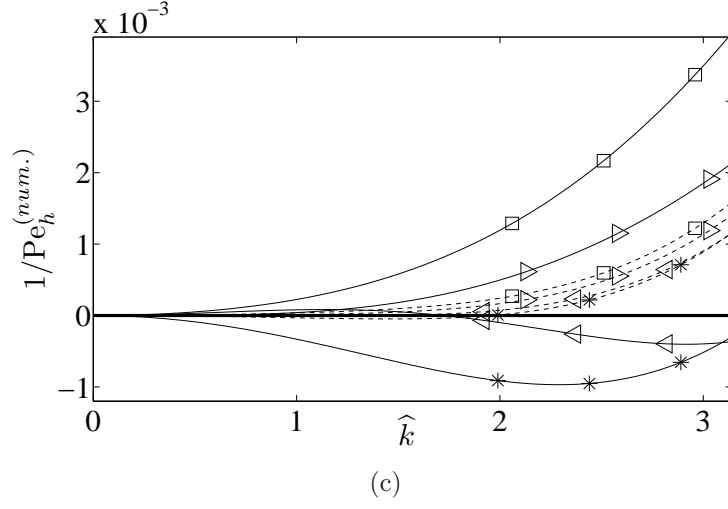
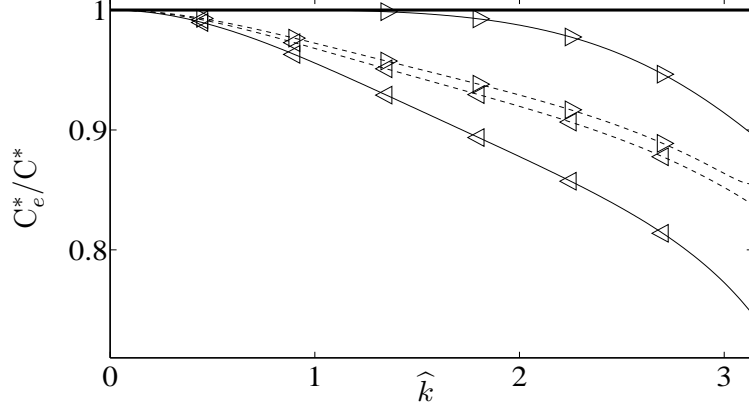


Figure 5: Distribution of the inverse numerical cell-Péclet number $1/\text{Pe}_h^{(num.)}$ with respect to the dimensionless wavenumber \hat{k} , at different values of C^* for (a) $P^e = 1$, (b) $P^e = 2$, (c) $P^e = 3$ and (d) $P^e = 4$. Symbol \triangleleft : element's leftmost node; symbol \triangleright : element's rightmost node; symbol $*$: element's left inner node (only for $P^e = 3$ and $P^e = 4$); symbol \square : element's right inner node (only for $P^e = 3$ and $P^e = 4$); symbol \circ : element's central node (only for $P^e = 2$ and $P^e = 4$). Dimensionless times $C^* = 1$ (solid line) and $C^* = 10$ (dashed line) are shown.

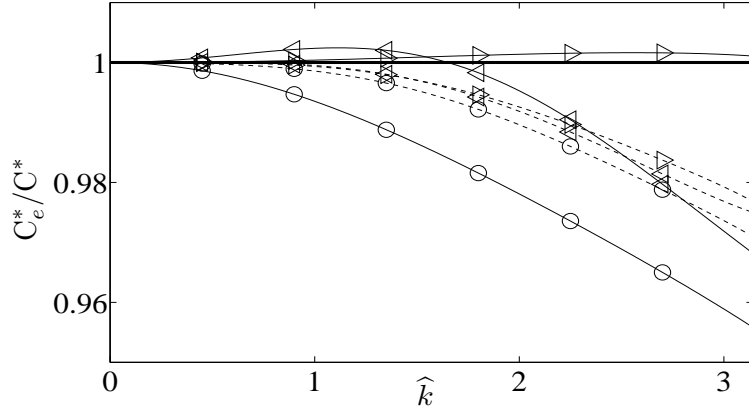
present Fourier analysis for the one-dimensional advection equation provides evidence that the numerical dissipation for the upwind nodes, introduced by



the simple upwind strategy followed for the advective numerical fluxes, may become negative in the high wavenumber range, as shown in figure 5. This feature may be of some concern when the proposed method is coupled with explicit time-stepping schemes. Nevertheless, the semi-discretized version of DCVFEM is stable for all considered orders of interpolation P^e , since the real parts of the eigenvalues of the amplification matrix are negative.



(a)

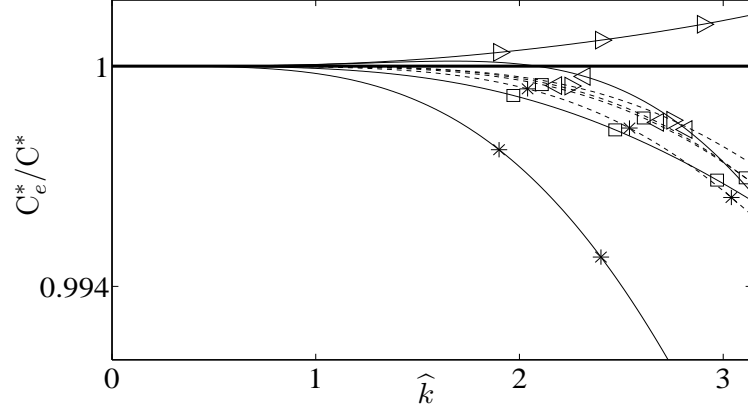


(b)

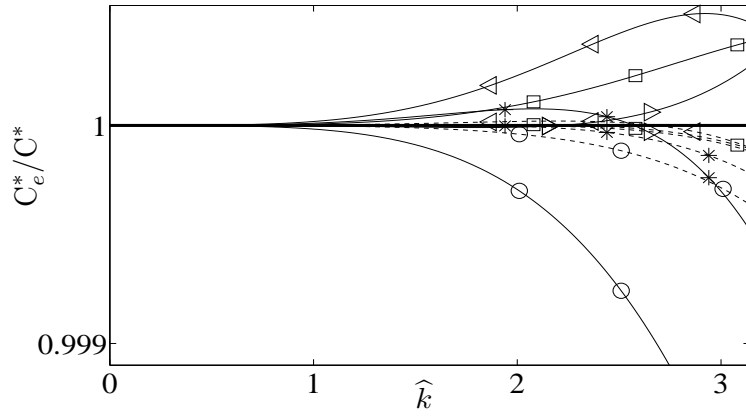
Figure 6: Distribution of the ratio C_e^*/C^* with respect to the dimensionless wavenumber \hat{k} , at different values of C^* for (a) $P^e = 1$, (b) $P^e = 2$, (c) $P^e = 3$ and (d) $P^e = 4$. Symbol \triangleleft : element's leftmost node; symbol \triangleright : element's rightmost node; symbol $*$: element's left inner node (only for $P^e = 3$ and $P^e = 4$); symbol \square : element's right inner node (only for $P^e = 3$ and $P^e = 4$); symbol \circ : element's central node (only for $P^e = 2$ and $P^e = 4$). Dimensionless times $C^* = 1$ (solid line) and $C^* = 10$ (dashed line) are shown.

5. Numerical simulation of selected problems

The accuracy of the proposed method is investigated by numerical tests and compared against GFEM and DGFEM calculations.



(c)



(d)

5.1. Steady, linear advection-diffusion

5.1.1. Homogeneous problem

The following steady, linear advection-diffusion problem is considered:

$$\begin{cases} \frac{\partial T}{\partial x} - \frac{\partial^2 T}{\partial x^2} = 0, & x \in (-1, 1) \\ T(-1) = e^{-1} \\ T(1) = e^1 \end{cases} \quad (50)$$

The analytical solution is $T(x) = e^x$. The \mathbb{L}^2 error norms of results for the DCVFEM and DGFEM, calculated on progressively refined uniform grids and with different orders of interpolation P^e , are reported in figure 7. The value of the parameter α in (27) is set to $\alpha = 10$. The errors are computed at the interpolation nodes for both the temperature T and the heat flux q , while errors at superconvergence nodes are computed only for the heat flux. The following conclusions can be drawn:

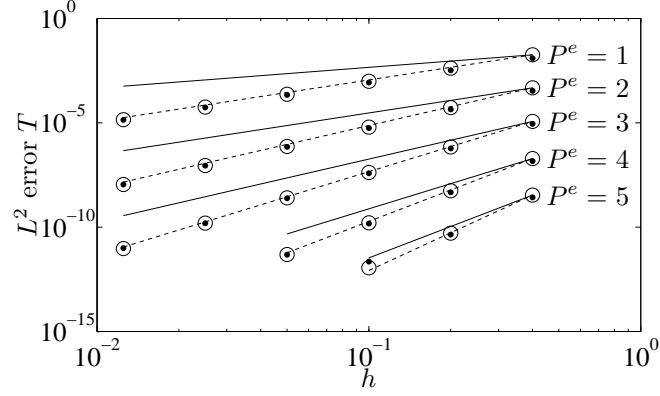
- The error on T decreases as h^{P^e+1} .
- The error on q computed at the interpolation nodes decreases as h^{P^e} .
- The error on q computed at the element's quadrature nodes, which are the zeros of the Legendre polynomial of order P^e , decreases as h^{P^e+1} .
- The errors on T, q computed with the mixed formulation of DGFEM are comparable to those of DCFEM.

5.1.2. Forced problem

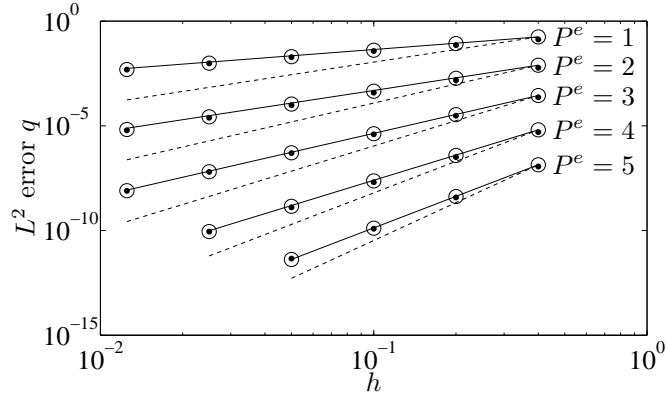
The Hemker problem [57, Appendix B] is defined as:

$$\left\{ \begin{array}{l} \frac{\mathrm{d}}{\mathrm{d}x}(uT) - D \frac{\mathrm{d}^2 T}{\mathrm{d}x^2} = Q(x), \quad x \in (-1, 1) \\ u(x) = x; \quad D = 10^{-10} \\ Q(x) = -D \pi^2 \cos(\pi x) - \pi x \sin(\pi x) \\ \qquad \qquad \qquad + \cos(\pi x) + \frac{\operatorname{erf} \frac{x}{\sqrt{2D}}}{1} \\ T(-1) = -2; \quad T(1) = 0 \end{array} \right. \quad (51)$$

This test-case is used to investigate the capability of the proposed methodology to resolve internal layers without generating unphysical oscillations, typical of the continuous formulations [57, Appendix B]. In figure 8(a) the classical continuous Galerkin formulation (GFEM) is used with $P^e = 5$ and $h = 0.1$. The solution reveals unphysical oscillations. The DGFEM and DCVFEM solutions are compared in figure 8(b) and (c) for $P^e = 2$ and $P^e = 5$, respectively, with $h = 0.1$. For both orders of accuracy used, there



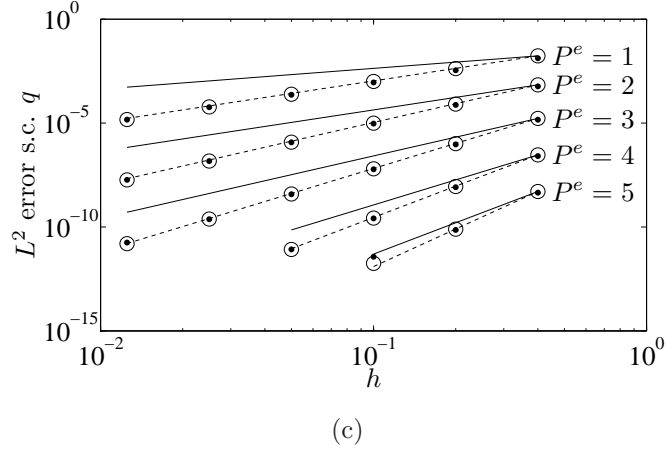
(a)



(b)

Figure 7: Error norm \mathbb{L}^2 for solution of problem (50) for (a) temperature T , (b) heat flux q and (c) superconvergence heat flux q for different polynomial order P^e . Symbol \circ : DCVFEM; symbol \bullet : DGFEM. For reference, lines of convergence rates P^e (solid line) and $P^e + 1$ (dashed line) are plotted.

is no evident difference between both computed solutions and the analytical solution and no evident unphysical oscillation. Figures 8(d) and 8(e), for $P^e = 2$ and $P^e = 5$, respectively, compare the errors for the two considered approaches at the interpolation nodes. The errors resulting from the two methods are of the same order of magnitude. In the case $P^e = 2$, the DGFEM performs slightly better, in general, but the DCVFEM yields smaller errors at the downstream nodes of each element. In the case $P^e = 5$, the error in proximity of the discontinuity is of one order of magnitude greater than in



the smooth region; the DCVFEM performs slightly better near the discontinuity, while in the smooth-solution region the DGFEM and DCVFEM errors are very similar.

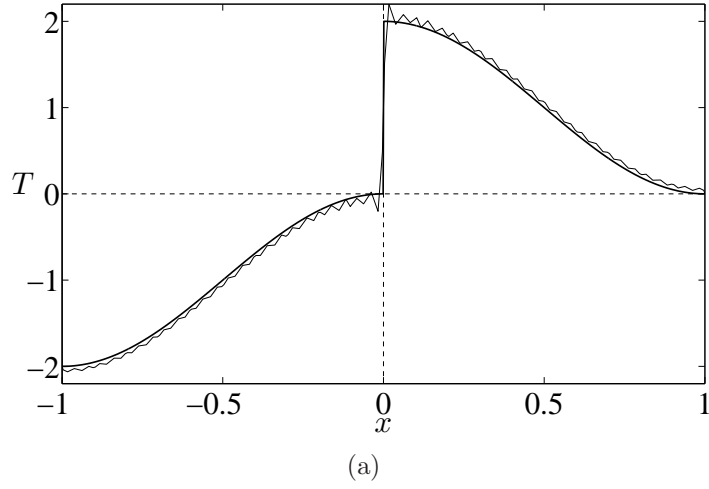
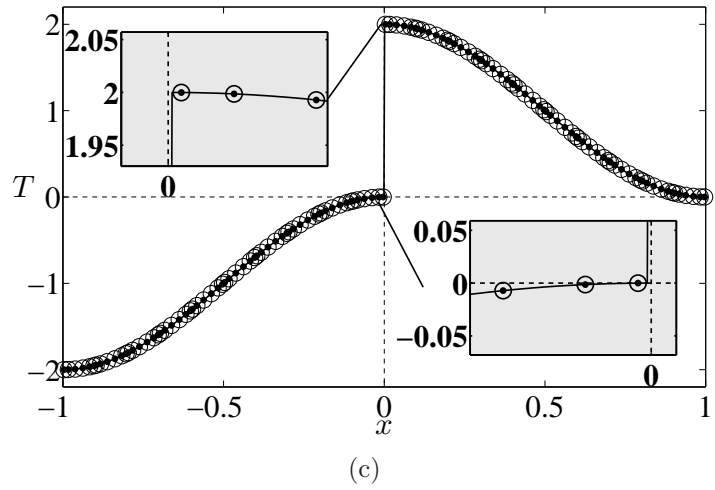
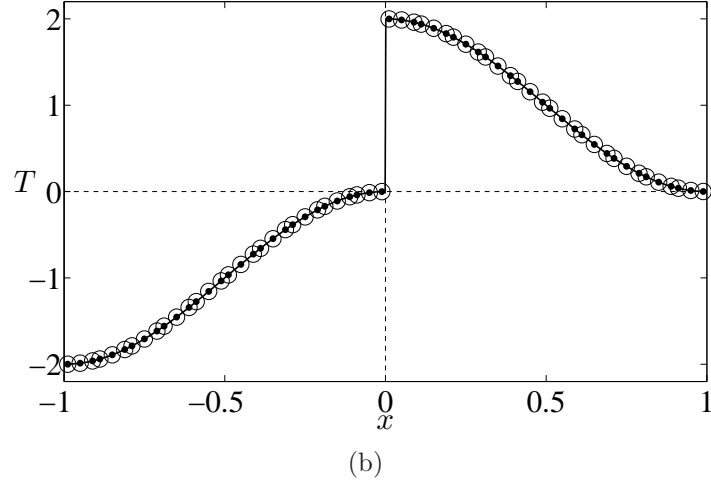


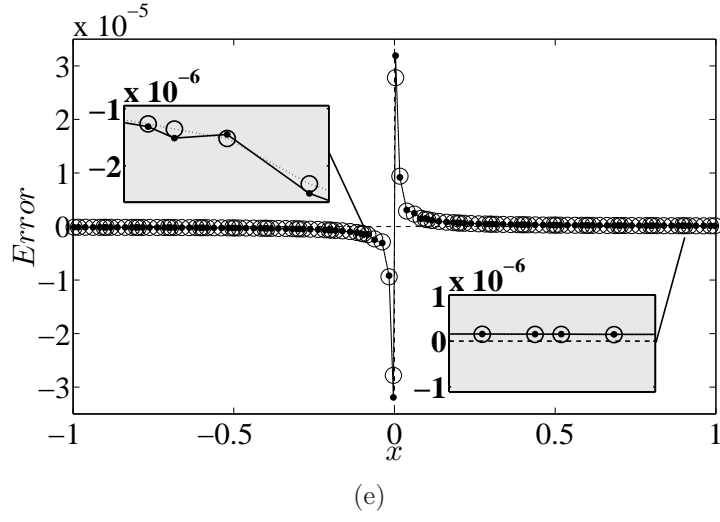
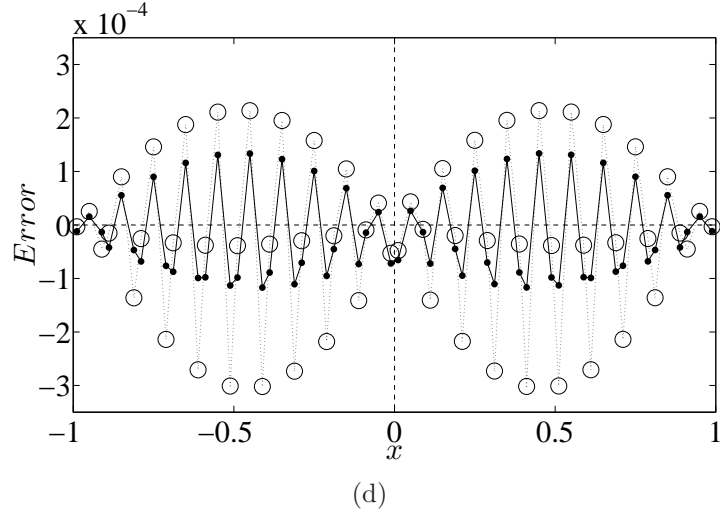
Figure 8: (a) GFEM (solid thin line), DCVFEM and DGFEM solutions of problem (51), compared to the analytic solution (solid thick line) for (b) $P^e = 2$ and (c) $P^e = 5$. Errors at interpolation nodes for the DCVFEM and DGFEM for (d) $P^e = 2$ and (e) $P^e = 5$. Symbol \circ : DCVFEM; symbol \bullet : DGFEM.



5.2. Steady, linear diffusion with discontinuous thermophysical properties

The following diffusion equation, with a distributed source term and Dirichlet boundary conditions, is solved in the case of discontinuous thermal conductivity D :

$$\begin{cases} \frac{d}{dx} \left(D \frac{dT}{dx} \right) + e^{8x} = 0 \\ T(x = -1) = 1 \\ T(x = 1) = -1 \end{cases} \quad (52)$$



The thermal conductivity takes two different values in the domain:

$$\begin{cases} D = 5 & \text{in } [-1, 0] \\ D = \frac{1}{2} & \text{in } (0, 1] \end{cases} \quad (53)$$

The analytical solution to problem (52,53) is:

$$\begin{cases} T(x) = \frac{\cosh(8)}{176} - \frac{e^{8x}}{320} - \frac{59x}{320} - \frac{x}{3520e^8} + \frac{xe^8}{352} + \frac{261}{320}, & x \in [-1, 0] \\ T(x) = \frac{\cosh(8)}{176} - \frac{e^{8x}}{32} - \frac{59x}{32} - \frac{x}{352e^8} + \frac{5xe^8}{176} + \frac{27}{32}, & x \in (0, 1] \end{cases} \quad (54)$$

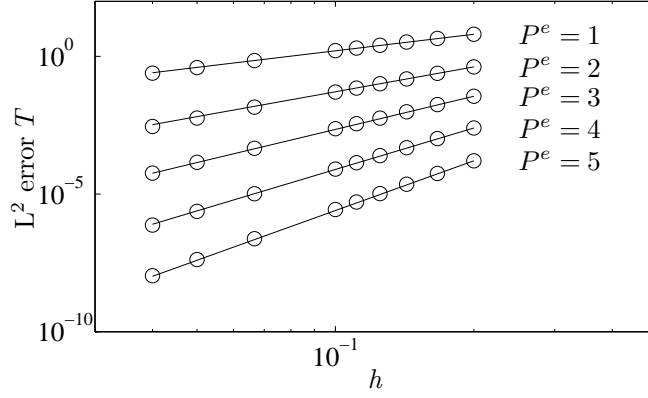
The problem is solved with the proposed DCVFEM on progressively refined uniform grids and different orders of interpolation. The calculated \mathbb{L}^2 error norms are reported in figure 9. The following conclusions can be drawn:

- The orders of convergence rate are $P^e + 1$, P^e and $2P^e$ for the temperature and the flux at the interpolation nodes and for the flux at the super-convergence nodes, respectively.
- The convergence rate for the flux obtained at the superconvergence nodes is noteworthy but, according to the outcomes of the other test-cases and the Fourier analysis, it can not be considered as a general result.
- In figure 9(c), the L_2 error for the heat flux, interpolated at the super-convergence points, shows an inconsistent behavior on the finest mesh for $P^e = 4$ and $P^e = 5$. This feature is compatible with the double-precision arithmetic used for the calculations and with the observation that the aforementioned inconsistency appears for values of the error of the order of 10^{-11} . Since the maximum analytical heat flux is approximately 331, the inconsistent behavior appears for relative errors of the order of $10^{-14} \div 10^{-15}$, which can be ascribed to the accumulation of round-off errors.

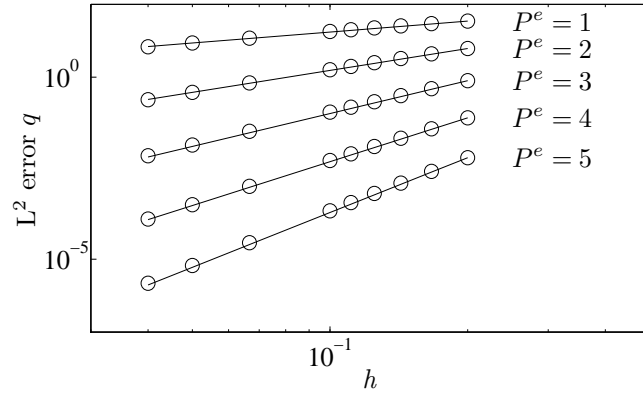
5.3. Burgers' equation

In order to test the capability of the proposed method to accurately represent high gradients, the periodic Burgers' equation is solved:

$$\begin{cases} \frac{\partial u}{\partial t} + \frac{\partial}{\partial x} \left(\frac{u^2}{2} \right) = \frac{1}{Re} \frac{\partial^2 u}{\partial x^2} \\ u(x, t) = u(x + 1, t) \\ u(x, 0) = \sin(2\pi x) \end{cases} \quad (55)$$



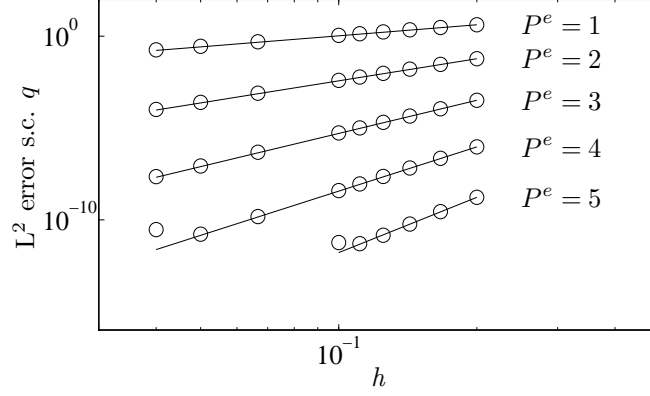
(a)



(b)

Figure 9: Error norm \mathbb{L}^2 for the solution of problem (52,53) for (a) temperature T , (b) heat flux q and (c) superconvergence heat flux q for different polynomial order P^e . Symbol \circ : DCVFEM. For reference, lines of convergence rate (a) $P^e + 1$, (b) P^e and (c) $2P^e$ are plotted (solid line).

Results by the proposed DCVFEM method are compared against reference solutions, obtained by the method proposed by Mittal and Singhal [35], and against the results by DGFEM. Figure 10 shows the solutions to problem (55) obtained with a mesh of size $h = 1/50$, with different polynomial orders P^e and for different values of the Reynolds number Re , at a final time $t = 2$. Error norms for DCVFEM and DGFEM are compared in table 1. The following conclusions can be drawn:



(c)

- The DCVFEM and DGFEM yield solutions of comparable accuracy in all considered cases.
- Considering that no flux-limiters nor adaptation strategies are employed, for high values of the Reynolds number ($Re = 10^4$ and $Re \rightarrow \infty$) both DCVFEM and DGFEM errors are not reduced significantly with increasing polynomial order P^e due to the Gibbs' phenomenon near the discontinuity.

5.4. Steady-state, two-dimensional diffusion with source term

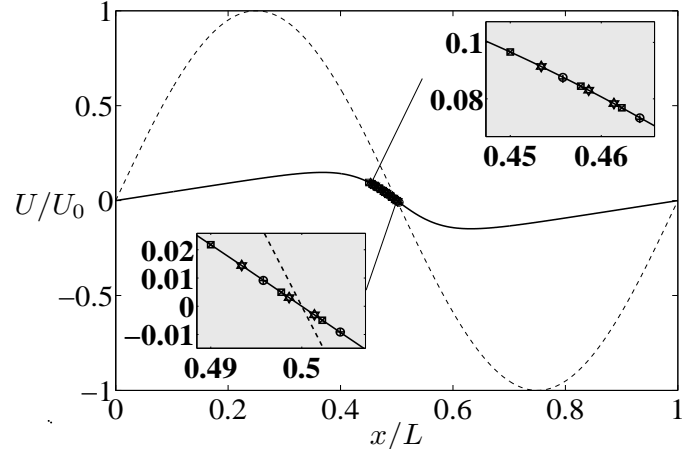
The stationary, two-dimensional diffusion problem with Dirichlet boundary conditions can be cast as:

$$\mathbf{q} = -\nabla T \quad (x, y) \in \Omega \quad (56a)$$

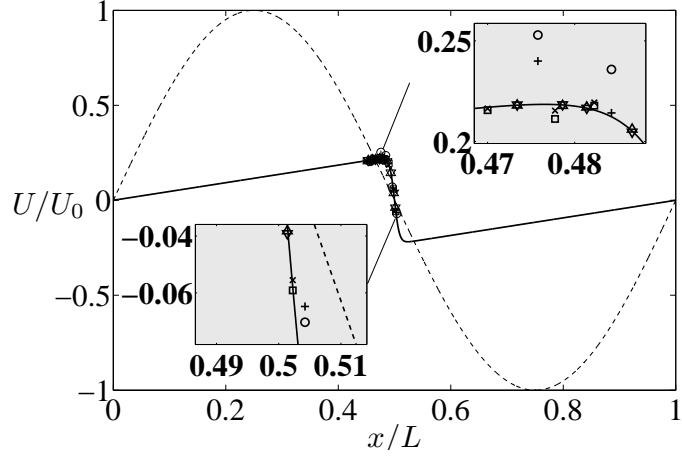
$$\nabla \cdot \mathbf{q} = Q(x, y) \quad (x, y) \in \Omega \quad (56b)$$

$$T = g(x, y) \quad (x, y) \in \partial\Omega \quad (56c)$$

where Ω is a simply-connected, open set with regular boundary $\partial\Omega$ and Q denotes the source term. Problem (56) is solved by the proposed methodology using quadrilateral, sub-parametric elements, where a bilinear coordinate transformation is used to map the physical space $(x, y) \in \Omega$ onto the



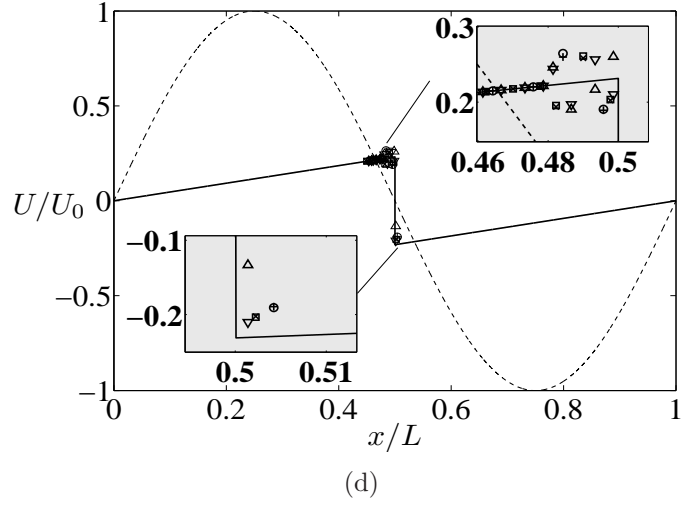
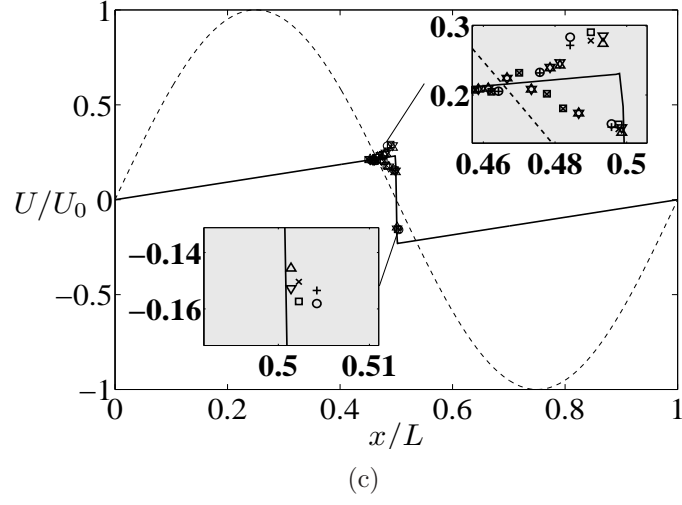
(a)



(b)

Figure 10: DCVFEM and DGFEM solutions of problem (55), compared to the reference solution (solid line) for (a) $Re = 10^2$, (b) $Re = 10^3$, (c) $Re = 10^4$ and (d) $Re \rightarrow +\infty$. Symbol \circ , \square and ∇ : DCVFEM with $P^e = 1, 2, 3$ respectively; Symbol $+$, \times and \triangle : DGFEM with $P^e = 1, 2, 3$ respectively. The initial condition (dashed line) is plotted for reference.

parametric space $(\xi, \eta) \in \hat{\Omega} \equiv [-1, 1] \times [-1, 1]$, while the approximation of T and \mathbf{q} is achieved by the tensor product of one-dimensional polynomial



interpolants $L_i(\xi)$ and $L_j(\eta)$, respectively:

$$\widehat{T}(\xi, \eta) = \sum_{i,j=1}^N T_{ij} L_i(\xi) L_j(\eta) \quad (57)$$

$$\widehat{\mathbf{q}}(\xi, \eta) = \sum_{i,j=1}^N \mathbf{q}_{ij} L_i(\xi) L_j(\eta) \quad (58)$$

Table 1: Error norms \mathbb{L}^2 and \mathbb{L}^∞ for the solution of problem (55) for DCVFEM and DGFEM with different polynomial order P^e and different values of the Reynolds number Re . All simulations have been made with a uniform mesh of size $h = 1/50$.

Re	P^e	DCVFEM		DGFEM	
		\mathbb{L}^2 error	\mathbb{L}^∞ error	\mathbb{L}^2 error	\mathbb{L}^∞ error
10^2	1	1.93E-04	4.31E-04	2.24E-04	6.49E-04
	2	6.25E-06	2.93E-05	6.37E-06	2.96E-05
	3	1.75E-06	4.70E-06	2.38E-06	7.68E-06
10^3	1	7.56E-03	3.45E-02	6.23E-03	3.81E-02
	2	1.38E-03	9.15E-03	6.30E-04	3.78E-03
	3	2.95E-04	2.90E-03	2.83E-04	2.02E-03
10^4	1	1.34E-02	7.15E-02	1.29E-02	7.61E-02
	2	1.28E-02	7.48E-02	1.26E-02	8.18E-02
	3	1.05E-02	6.32E-02	1.03E-02	7.03E-02
$\rightarrow +\infty$	1	7.91E-03	4.03E-02	7.58E-03	4.02E-02
	2	5.95E-03	3.41E-02	5.93E-03	3.13E-02
	3	4.94E-03	2.82E-02	1.03E-02	9.75E-02

where $N = P^e + 1$. The one-dimensional coordinates of the $N \times N$ interpolation nodes (ξ_i, η_j) are the zeros of the Legendre polynomial of order N . The control-volumes V_{ij} are defined in (ξ, η) space by partitioning $\widehat{\Omega}$ into a collection of rectangles:

$$V_{ij} = \{(\xi, \eta) \mid a_{i-1} \leq \xi \leq a_i, a_{j-1} \leq \eta \leq a_j\}, \quad i, j = 1, \dots, N \quad (59)$$

where a_i , $1 \leq i \leq N - 1$ are the roots of the Legendre polynomial of order $N - 1$, while $a_0 = -1$, $a_N = 1$. A sketch of the resulting partition of an element with $P^e = 2$ in transformed space is shown in figure 12.

The problem (56) is solved on $\Omega = [0, 1] \times [0, 1]$ with

$$Q = -[2 - 4\pi^2 x(x - 1)] \cos(2\pi y) \quad (60)$$

Homogeneous Dirichlet boundary conditions $T = 0$ are enforced on the boundary $\{0, 1\} \times [0, 1]$ and periodic conditions hold along y . The analytical solution is

$$T(x, y) = x(x - 1) \cos(2\pi y) \quad (61)$$

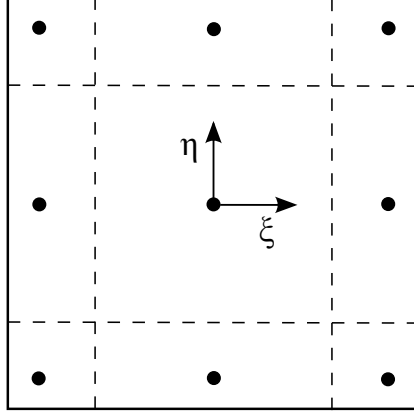


Figure 12: Sketch of the subdivision of an element with $P^e = 2$ into control volumes, in transformed (ξ, η) space. Dots: interpolation nodes, dashed lines: control volume boundary.

Figure 13 shows the convergence rate attained for the scalar field T by the proposed method with $C_{11} = 10$ in (27), for different polynomial orders of interpolation P^e and for both a regular, Cartesian mesh and a randomly distorted mesh. The maximum absolute error e on the interpolation nodes is considered. e_0 denotes the *reference* error, computed on a uniform, Cartesian 10×10 mesh. On sufficiently refined meshes, both uniform and random, the maximum absolute error scales as h^{P^e+1} , where h is the mesh diameter.

6. Concluding remarks

The discontinuous control-volume finite-element method is applied to the one-dimensional advection-diffusion equation and to the two-dimensional diffusion equation. The mixed-formulation approach is followed, consisting in approximating the weak formulation of both the constitutive and the conservation equations, without *merging* them into the *fundamental* equation. A formal derivation of the method is provided and the regularity conditions for the existence of the weak form of the problem are investigated. Expressions for the numerical traces are inherited from the DGFEM literature: the numerical advective flux is expressed by a simple upwinding [26], while the numerical diffusive flux is represented by the LDG method [13]. Both P - and h -convergence are verified in different test-cases, dealing with steady linear diffusion, steady advection-diffusion and the (non-linear) Burger's equation.

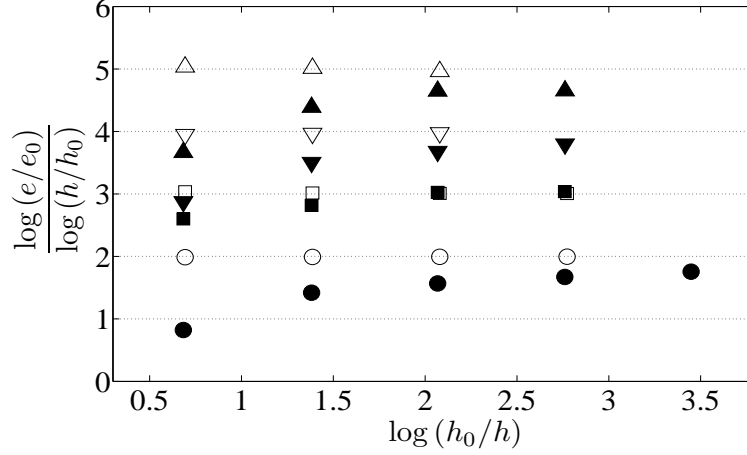


Figure 13: Convergence rate for the solution of problem (56) with $C_{11} = 10$. Void symbols: uniform, Cartesian meshes. Filled symbols: random meshes. Symbols as follows: \circ : $P^e = 1$, \square : $P^e = 2$, ∇ : $P^e = 3$ and \triangle : $P^e = 4$.

A preliminary test for the extension of the method to the multi-dimensional case is made by solving a two-dimensional diffusion problem with quadrilateral elements. The Fourier analysis is used to confirm the numerical results, to investigate the dispersion and dissipation characteristics of the proposed method and to deduce the influence of the coefficient α (see eq. (27)) for different values of P^e . The dissipation error provided by the DCVFEM is considerably smaller than the corresponding error resulting from GFEM and finite-difference approximations. However, during the early stages of evolution in time, the DCVFEM solution is affected by dispersion, differently from the GFEM and finite-difference results. The Fourier analysis of the advection problem reveals that the DCVFEM method yields both dissipation and dispersion errors, where the numerically-simulated Fourier modes are progressively damped and travel slower than the exact solution.

A. Details of the Fourier analysis

The details for the Fourier analysis are reported for the case of $P^e = 1$, matrices are reported for the case $P^e = 2$ as well. The procedure can be easily extended to the cases $P^e = 2, 3, 4$, but some calculations must be carried out numerically as their inherent complexity prevents using the symbolic manipulation. Each element endows $P^e + 1$ nodes and $P^e + 1$ control volumes,

the nodes are equally-spaced in the domain. The j -th node in the e -th element is located at

$$\begin{aligned}\{x_{e,j}^*\}_{j=1}^2 &= \left\{x_e^* - \frac{1}{4}, x_e^* + \frac{1}{4}\right\} & (P^e = 1) \\ \{x_{e,j}^*\}_{j=1}^3 &= \left\{x_e^* - \frac{1}{3}, x_e^*, x_e^* + \frac{1}{3}\right\} & (P^e = 2)\end{aligned}\tag{A.1}$$

A.1. Unsteady diffusion

Application of the proposed DCVFEM to problem (32) yields the following set of algebraic equations for the e -th element:

$$\begin{cases} \mathbf{M} \mathbf{q}_e^* = \mathbf{A} \boldsymbol{\theta}_{e-1} + \mathbf{B} \boldsymbol{\theta}_e + \mathbf{C} \boldsymbol{\theta}_{e+1} \\ \mathbf{M} \frac{d\boldsymbol{\theta}_e}{d\text{Fo}_h} = \mathbf{D} \boldsymbol{\theta}_{e-1} + \mathbf{E} \boldsymbol{\theta}_e + \mathbf{F} \boldsymbol{\theta}_{e+1} \\ \quad + \mathbf{A} \mathbf{q}_{e-1}^* + \mathbf{B} \mathbf{q}_e^* + \mathbf{C} \mathbf{q}_{e+1}^* \end{cases}\tag{A.2a}$$

where \mathbf{q}_e^* and $\boldsymbol{\theta}_e$ are $(P^e + 1)$ -component vectors containing the element's nodal values of q_h^* and θ_h , respectively. The coefficient matrices appearing in (A.2) for the linear case are:

$$\begin{aligned}\mathbf{M} &= \frac{1}{2} \begin{bmatrix} 1 & 0 \\ 0 & 1 \end{bmatrix} & \mathbf{A} &= \frac{1}{4} \begin{bmatrix} -1 & 3 \\ 0 & 0 \end{bmatrix} & \mathbf{B} &= \frac{1}{4} \begin{bmatrix} 1 & -3 \\ 3 & -1 \end{bmatrix} \\ \mathbf{C} &= \frac{1}{4} \begin{bmatrix} 0 & 0 \\ -3 & 1 \end{bmatrix} & \mathbf{D} &= \frac{C_{11}^*}{2} \begin{bmatrix} -1 & 3 \\ 0 & 0 \end{bmatrix} \\ \mathbf{E} &= \frac{C_{11}^*}{2} \begin{bmatrix} -3 & 1 \\ 1 & -3 \end{bmatrix} & \mathbf{F} &= \frac{C_{11}^*}{2} \begin{bmatrix} 0 & 0 \\ 3 & -1 \end{bmatrix}\end{aligned}\tag{A.3}$$

while for the parabolic case are:

$$\begin{aligned}
\mathbf{M} &= \frac{1}{48} \begin{bmatrix} 15 - \sqrt{3} & 6 - 6\sqrt{3} & 3 - \sqrt{3} \\ 2\sqrt{3} & 12\sqrt{3} & 2\sqrt{3} \\ 3 - \sqrt{3} & 6 - 6\sqrt{3} & 15 - \sqrt{3} \end{bmatrix} \\
\mathbf{A} &= \frac{1}{16} \begin{bmatrix} 3 & -10 & 15 \\ 0 & 0 & 0 \\ 0 & 0 & 0 \end{bmatrix} \quad \mathbf{B} \approx \frac{1}{8} \begin{bmatrix} 1.04 & -7 & 1.96 \\ 6.93 & 0 & -6.93 \\ -1.96 & 7 & -1.04 \end{bmatrix} \\
\mathbf{C} &= \frac{1}{16} \begin{bmatrix} 0 & 0 & 0 \\ 0 & 0 & 0 \\ -15 & 10 & -3 \end{bmatrix} \quad \mathbf{D} = \frac{C_{11}^*}{8} \begin{bmatrix} 3 & -10 & 15 \\ 0 & 0 & 0 \\ 0 & 0 & 0 \end{bmatrix} \\
\mathbf{E} &= \frac{C_{11}^*}{8} \begin{bmatrix} -15 & 10 & -3 \\ 0 & 0 & 0 \\ -3 & 10 & -15 \end{bmatrix} \quad \mathbf{F} = \frac{C_{11}^*}{8} \begin{bmatrix} 0 & 0 & 0 \\ 0 & 0 & 0 \\ 15 & -10 & 3 \end{bmatrix}
\end{aligned} \tag{A.4}$$

Due to the relaxation of the inter-element continuity, the equations for the element's nodes are different [55]. There are $P^e + 1$ independent sequences of nodal equations to be considered. The independent sequences for the element's nodal values q_h^* and θ_h are denoted as:

$$\{q_{e,j}^*(\text{Fo}_h)\}_{e=0}^{N-1} \quad \{\theta_{e,j}(\text{Fo}_h)\}_{e=0}^{N-1} \tag{A.5}$$

Taking the DFT [48] of (A.5) yields the Fourier coefficients $Q_{k,j}(\text{Fo}_h)$ and $\Theta_{k,j}(\text{Fo}_h)$, for $k = 0, \dots, N-1$:

$$Q_{k,j}(\text{Fo}_h) = \sum_{e=0}^{N-1} q_{e,j}^*(\text{Fo}_h) W(-\widehat{k}x_{e,j}^*) \tag{A.6a}$$

$$\Theta_{k,j}(\text{Fo}_h) = \sum_{e=0}^{N-1} \theta_{e,j}(\text{Fo}_h) W(-\widehat{k}x_{e,j}^*) \tag{A.6b}$$

In relations (A.5,A.6) $j = 1, 2$ in the linear case $P^e = 1$, $j = 1, 2, 3$ in the parabolic case $P^e = 2$, and so on for increasing polynomial order P^e . The

vectors \mathbf{q}_e^* and $\boldsymbol{\theta}_e$ can be obtained from (A.6) using the inverse DFT [48], yielding, in the linear case:

$$\begin{aligned}\boldsymbol{\theta}_e &= \frac{1}{N} \sum_{k=0}^{N-1} \left\{ \begin{array}{c} \Theta_{k,1}(\text{Fo}_h) W(-\widehat{k}/4) \\ \Theta_{k,2}(\text{Fo}_h) W(\widehat{k}/4) \end{array} \right\} W(-\widehat{k}x_e^*) \\ &\equiv \frac{1}{N} \sum_{k=0}^{N-1} \mathbf{S}_k \boldsymbol{\Theta}_k(\text{Fo}_h) W(-\widehat{k}x_e^*)\end{aligned}\quad (\text{A.7a})$$

$$\begin{aligned}\mathbf{q}_e^* &= \frac{1}{N} \sum_{k=0}^{N-1} \left\{ \begin{array}{c} \mathbf{Q}_{k,1}(\text{Fo}_h) W(-\widehat{k}/4) \\ \mathbf{Q}_{k,2}(\text{Fo}_h) W(\widehat{k}/4) \end{array} \right\} W(-\widehat{k}x_e^*) \\ &\equiv \frac{1}{N} \sum_{k=0}^{N-1} \mathbf{S}_k \mathbf{Q}_k(\text{Fo}_h) W(-\widehat{k}x_e^*)\end{aligned}\quad (\text{A.7b})$$

where

$$\boldsymbol{\Theta}_k(\text{Fo}_h) \equiv \left\{ \begin{array}{c} \Theta_{k,1}(\text{Fo}_h) \\ \Theta_{k,2}(\text{Fo}_h) \end{array} \right\} \quad (\text{A.8a})$$

$$\mathbf{Q}_k(\text{Fo}_h) \equiv \left\{ \begin{array}{c} \mathbf{Q}_{k,1}(\text{Fo}_h) \\ \mathbf{Q}_{k,2}(\text{Fo}_h) \end{array} \right\} \quad (\text{A.8b})$$

and the *shift* operator is

$$\mathbf{S}_k \equiv \begin{bmatrix} W(-\widehat{k}/4) & 0 \\ 0 & W(\widehat{k}/4) \end{bmatrix} \quad (\text{A.9})$$

Similar expressions are obtained for the parabolic case and higher polynomial orders. Substituting (A.7) into (A.2) and taking into account the orthogonality of the Fourier modes, yields:

$$\left\{ \begin{array}{l} \mathbf{M} \mathbf{Q}_k = \left(\mathbf{A} W(-\widehat{k}) + \mathbf{B} + \mathbf{C} W(\widehat{k}) \right) \boldsymbol{\Theta}_k \\ \mathbf{M} \frac{d\boldsymbol{\Theta}_k}{d\text{Fo}_h} = \left(\mathbf{D} W(-\widehat{k}) + \mathbf{E} + \mathbf{F} W(\widehat{k}) \right) \boldsymbol{\Theta}_k \\ \quad + \left(\mathbf{A} W(-\widehat{k}) + \mathbf{B} + \mathbf{C} W(\widehat{k}) \right) \mathbf{Q}_k \end{array} \right. \quad (\text{A.10a})$$

$$(\text{A.10b})$$

Eliminating \mathbf{Q}_k using equation (A.10a) yields to a system of ordinary differential equations for $\mathbf{\Theta}_k$:

$$\frac{d\mathbf{\Theta}_k}{d\text{Fo}_h} = \mathbf{G}(\hat{k}) \mathbf{\Theta}_k \quad (\text{A.11})$$

where \mathbf{G} can be regarded as the amplification matrix for the method.

The calculated solution $\mathbf{\Theta}_k$ to system (A.11) (see eq. (35)) is Taylor expanded with respect to \hat{k} , yielding, in the linear case:

$$\mathbf{\Theta}_k = \begin{pmatrix} W\left(-\frac{\hat{k}}{4}\right) + O(\hat{k}^2) \\ W\left(\frac{\hat{k}}{4}\right) + O(\hat{k}^2) \end{pmatrix} e^{-\hat{k}^2 \text{Fo}_h} \quad (\text{A.12})$$

which, compared with the DFT of the analytical solution (34), sampled at the nodal points,

$$\mathbf{\Theta}_k^{(an.)} = \begin{pmatrix} W\left(-\frac{\hat{k}}{4}\right) \\ W\left(\frac{\hat{k}}{4}\right) \end{pmatrix} e^{-\hat{k}^2 \text{Fo}_h} \quad (\text{A.13})$$

shows that the method is second-order accurate.

The Fourier modes for the flux \mathbf{Q}_k can now be obtained from the constitutive equation (A.10a). A Taylor series expansion with respect to \hat{k} yields, in the linear case:

$$\mathbf{Q}_k = -i\hat{k} \begin{pmatrix} W\left(-\frac{\hat{k}}{4}\right) + O(\hat{k}) \\ W\left(\frac{\hat{k}}{4}\right) + O(\hat{k}) \end{pmatrix} e^{-\hat{k}^2 \text{Fo}_h} \quad (\text{A.14})$$

which, compared with the DFT of the analytical flux, sampled at the nodes,

$$\mathbf{Q}_k^{(an.)} = -i\hat{k} \begin{pmatrix} W\left(-\frac{\hat{k}}{4}\right) \\ W\left(\frac{\hat{k}}{4}\right) \end{pmatrix} e^{-\hat{k}^2 \text{Fo}_h} \quad (\text{A.15})$$

shows that the computed flux is first order accurate. The element's mid-point is the superconvergence point for a linear element [56, ch.14]. Linear interpolation of the computed flux at this point yields

$$\left(-i\widehat{k} + O(\widehat{k}^2)\right) e^{-\widehat{k}^2 \text{Fo}_h} \quad (\text{A.16})$$

which is a second-order accurate approximation of the analytical flux at the same point.

A.2. Unsteady advection

The application of the proposed DCVFEM to problem (44) leads to the following expression for the discrete Fourier transform of θ :

$$\dot{\Theta}_k = \left(\mathbf{U}_l W(-\widehat{k}) + \mathbf{U}_c\right) \Theta_k \equiv \mathbf{G} \Theta_k \quad (\text{A.17})$$

where \mathbf{G} is regarded as the amplification matrix for the semi-discrete equation. The coefficient matrices appearing in (A.17) for the linear case are:

$$\mathbf{U}_l = \begin{bmatrix} -1 & 3 \\ 0 & 0 \end{bmatrix} \quad \mathbf{U}_c = \begin{bmatrix} -1 & -1 \\ 2 & -2 \end{bmatrix} \quad (\text{A.18})$$

and for the parabolic case are:

$$\mathbf{U}_l = \frac{1}{16} \begin{bmatrix} 21 & -70 & 105 \\ -3 & 10 & -15 \\ -3 & 10 & -15 \end{bmatrix} \quad \mathbf{U}_c = \frac{1}{16} \begin{bmatrix} -33 & -26 & 3 \\ 39 & -10 & -21 \\ -9 & 86 & -69 \end{bmatrix} \quad (\text{A.19})$$

The calculated solution Θ_k to system (A.17) (see eq.(46)) is Taylor expanded with respect to \widehat{k} , yielding, in the linear case:

$$\Theta_k = \begin{pmatrix} W\left(-\frac{\widehat{k}}{4}\right) \\ W\left(\frac{\widehat{k}}{4}\right) \end{pmatrix} W(-\widehat{k}C^*) + O(\widehat{k}^2) \quad (\text{A.20})$$

which is a second-order accurate approximation of $\Theta_k^{(\text{an.})}$, that is, the DFT of the analytic solution (45) sampled at the nodes.

References

- [1] J. D. Anderson. *Computational fluid dynamics*. McGraw Hill, New York, 1995.
- [2] D. N. Arnold, F. Brezzi, B. Cockburn and L. D. Marini. Unified analysis of discontinuous Galerkin methods for elliptic problems. *SIAM Journal on Numerical Analysis*, Vol. 39, No. 5, pp.1749–1779, 2002.
- [3] I. Babuška and M. Zlámal. Nonconforming elements in the finite element method with penalty. *SIAM J. Numer. Anal.*, Vol. 10, pp.863–875, 1979.
- [4] B. R. Baliga and S. V. Patankar. A new finite-element formulation for convection-diffusion problems. *Numerical Heat Transfer, Part B: Fundamentals*, Vol. 3, No. 4, pp.393–409, 1980.
- [5] J. Banaszek. Comparison of control volume and Galerkin finite element methods for diffusion-type problems. *Numerical Heat Transfer, Part B: Fundamentals*, Vol. 16, No. 1, pp.59–78, 1989.
- [6] F. Bassi and S. Rebay. A high-order accurate discontinuous finite element method for the numerical solution of the compressible Navier-Stokes equations. *J. Comput. Phys.*, Vol. 131, pp.267–279, 1997.
- [7] F. Bassi, S. Rebay, G. Mariotti, S. Pedinotti, M. Savini. A high-order accurate discontinuous finite element method for inviscid and viscous turbomachinery flows. *Proceedings of Second European Conference on Turbomachinery*, Vol. 1, Technologisch Instituut, Antwerpen, Belgium, pp.99–108, 1997.
- [8] F. Brezzi, D. Marini, P. Pietra and A. Russo. Discontinuous Galerkin approximations for elliptic problems. *Numer. Methods Partial Differential Equations*, Vol. 16, pp.365–378, 2000.
- [9] G. F. Carey and M. Utku. Stability of penalty finite-element methods for nonconforming problems. *Numerical Methods for Partial Differential Equations*, Vol. 2, pp.13–29, 1986.
- [10] P. Castillo, B. Cockburn, I. Perugia, D. Schotzau. An a priori error analysis of the local discontinuous Galerkin method for elliptic problems. *SIAM Journal on Numerical Analysis*, Vol. 38, pp. 16761706, 2000.

- [11] B. J. Choi, M. Iskandarani, J. C. Levin and D. B. Haidvogel. A spectral finite volume method for the shallow water equations. *Monthly Weather Review*, Vol. 132, No. 7, pp.1777–1791, 2004.
- [12] P. C. Ciarlet. Discrete maximum principle for finite difference operators. *AEQ. Math.*, Vol. 4, pp.338–352, 1970.
- [13] B. Cockburn and C. W. Shu. The local discontinuous Galerkin method for time-dependent convection-diffusion systems. *SIAM Journal on Numerical Analysis*, Vol. 35, pp.2440–2463, 1998.
- [14] B. Cockburn. Discontinuous Galerkin methods. *Journal of Applied Mathematics and Mechanics*, Vol. 83, No. 11, pp.731–754, 2003.
- [15] M. Fortin and F. Brezzi. *Mixed and hybrid finite element methods*. Springer Series in Computational Mathematics, Springer–Verlag, Berlin, 1991.
- [16] J. Giannakouros and G. E. Karniadakis. Spectral element-FCT method for scalar hyperbolic conservation laws. *Int. J. Numer. Methods Fluids*, Vol. 14, pp.707–727, 1992.
- [17] J. Giannakouros and G. E. Karniadakis. A spectral element-FCT method for the compressible Euler equations. *J. Comp. Phys.*, Vol. 115, No. 1, pp.65–85, 1994.
- [18] M. W. Hecht, F. O. Bryan, W. R. Holland. Upwind-weighted advection schemes for ocean tracer transport: an evaluation in a passive tracer context. *J. Geophys. Res.*, Vol. 103(C2), pp.3301–3321, 1995.
- [19] F. Q. Hu, M. Y. Hussaini, P. Rasetarinera. An analysis of the discontinuous Galerkin method for wave propagation problems. *J. Comp. Phys.*, Vol. 151, pp.921–946, 1999.
- [20] M. Iskandarani, J. C. Levin, B. J. Choi and D. B. Haidvogel. Comparison of advection schemes for high-order h–p finite element and finite volume methods. *Ocean Modelling*, Vol. 10, pp.233–252, 2004.
- [21] R. Kannan and Z. J. Wang. A Study of viscous flux formulations for a p-multigrid spectral volume Navier Stokes solver. *J. Sci. Comp.*, Vol. 41, pp.165–199, 2009.

- [22] R. Kannan and Z. J. Wang. The direct discontinuous Galerkin (DDG) viscous flux scheme for the high order spectral volume method. *Computers & Fluids*, Vol. 39, pp.2007–2021, 2010.
- [23] R. Kannan and Z. J. Wang. LDG2: A variant of the LDG viscous flux formulation for the spectral volume method. *J. Sci. Comp.*, Vol. 46, pp.314-328, 2011.
- [24] G. E. Karniadakis and S. J. Sherwin. *Spectral/hp element methods for CFD*. Oxford University Press, Oxford, 2005.
- [25] B. van Leer and M. Lo. A discontinuous Galerkin method for diffusion based on recovery. 18th AIAA Computational Fluid Dynamics Conference, AIAA 2007-4083, 2007.
- [26] B. Q. Li. *Discontinuous finite elements in fluid dynamics and heat transfer*. Springer-Verlag, Berlin, 2006.
- [27] George, Alan and Joseph Liu. *Computer Solution of Large Sparse Positive Definite Systems*. Prentice-Hall, 1981.
- [28] H. Liu and J. Yan. The direct discontinuous Galerkin (DDG) methods for diffusion problems. *SIAM Journal on Numerical Analysis*, Vol. 47, No.1, pp.675-698.
- [29] H. Liu and J. Yan. The direct discontinuous Galerkin (DDG) method for diffusion with interface corrections. *Commun. Comput. Phys.*, Vol. 8, No. 3, pp.541-564.
- [30] Y. Liu, M. Vinokur, Z. J. Wang. Spectral (finite) volume method for conservation laws on unstructured grids. V: extension to three-dimensional systems. *J. Comp. Phys.*, Vol. 212, pp.454–472, 2006.
- [31] Y. Liu, M. Vinokur, Z. J. Wang. Spectral difference method for unstructured grids I: basic formulation. *J. Comp. Phys.*, Vol. 216, pp.780–801, 2006.
- [32] H. Lomax, T. Pulliam and D. W. Zingg. *Fundamentals of computational fluid dynamics*. Springer-Verlag, Berlin, 2001.

- [33] M. J. Martinez. Comparison of Galerkin and control volume finite element for advection-diffusion problems. *Int. J. Numer. Meth. Fluids*, Vol. 50, pp.347–376, 2006.
- [34] C. Masson and H. J. Saabas and B. R. Baliga. Co-located equal-order control-volume finite element method for two-dimensional axisymmetric incompressible fluid flow. *Int. J. Numer. Meth. Fluids*, Vol. 18, pp.1–26, 1994.
- [35] R. C. Mittal and P. Singhal. Numerical solutions of periodic Burgers equation. *Indian J. pure appl. Math.*, Vol. 27, No. 7, pp.689–700, 1996.
- [36] M. Parsani, G. Ghorbaniasl, C. Lacor, E. Turkel. An implicit high-order spectral difference approach for large eddy simulation. *J. Comp. Phys.*, Vol. 229(14), pp.5373–5393, 2010.
- [37] S. V. Patankar. *Numerical heat transfer and fluid flow*. Taylor & Francis, New York, 1980.
- [38] A. Quarteroni and A. Valli. *Numerical approximation of partial differential equations*. Springer-Verlag Italia, Milano, 1994.
- [39] W. H. Reed and T. R. Hill. Triangular mesh methods for the neutron transport equation. *Tech. Report LA-UR-73-479*, Los Alamos Scientific Laboratory, Los Alamos, NM, 1973.
- [40] S. Salsa. *Partial differential equations in action*. Springer Verlag, Berlin, 2007.
- [41] G. E. Schneider and M. J. Raw. A skewed, positive influence coefficient upwinding procedure for control-volume-based finite-element convection-diffusion computation. *Numerical Heat Transfer, Part B: Fundamentals*, Vol. 9, No. 1, pp.1–26, 1986.
- [42] D. Sidilkover and G. E. Karniadakis. Spectral element-FCT method for the one- and two-dimensional compressible Euler equations. *Comput. Methods Appl. Mech. Eng.*, Vol. 116, pp.113–121, 1994.
- [43] C. W. Shu. Total variation diminishing Runge-Kutta schemes. *SIAM Journal of Scientific and Statistical Computing*, Vol. 9, pp.1073–1084, 1988.

- [44] C. W. Shu. Different formulations of the discontinuous Galerkin method for the viscous terms. in *Advances in Scientific Computing*, Z. C. Shi, M. Mu, W. Xue, J. Zou (Eds.), Science Press, pp.144–145, 2001.
- [45] Y. Sun, Z. J. Wang, Y. Liu. Spectral (finite) volume method for conservation laws on unstructured grids. VI: extension to viscous flow. *J. Comp. Phys.*, Vol. 215, pp.41–58, 2006.
- [46] K. Van den Abeele and T. Broeckhoven and C. Lacor. Dispersion and dissipation properties of the 1D spectral volume method and application to a p-multigrid algorithm. *J. Comp. Phys.*, Vol. 224, pp.616–636, 2007.
- [47] K. Van den Abeele, C. Lacor, Z. J. Wang. On the connection between the spectral volume and the spectral difference method. *J. Comp. Phys.*, Vol. 227(2), pp.877–885, 2007.
- [48] J. S. Walker. *Fast Fourier transforms. Second edition*. CRC Press, Boca Raton, 1996.
- [49] Z. J. Wang. Spectral (finite) volume method for conservation laws on unstructured grids: basic formulation. *J. Comp. Phys.*, Vol. 178, pp.210–251, 2002.
- [50] Z. J. Wang, Y. Liu. Spectral (finite) volume method for conservation laws on unstructured grids. II: extension to two-dimensional scalar equation. *J. Comp. Phys.*, Vol. 179, p.665, 2002.
- [51] Z. J. Wang, Y. Liu. Spectral (finite) volume method for conservation laws on unstructured grids. III: extension to one-dimensional systems. *J. Sci. Comput.*, Vol. 20, p.137, 2004.
- [52] Z. J. Wang, Y. Liu. Spectral (finite) volume method for conservation laws on unstructured grids. IV: extension to two-dimensional Euler equations. *J. Comp. Phys.*, Vol. 194, p.716, 2004.
- [53] Z. J. Wang, Y. Liu. Extension of the spectral volume method to high-order boundary representation. *J. Comp. Phys.*, Vol. 211, 154–178, 2006.
- [54] S. T. Zalesak. Fully multidimensional flux-corrected transport algorithms for fluids. *J. Comp. Phys.*, Vol. 31, pp.335–362, 1979.

- [55] M. Zhang and C. W. Shu. An analysis of three different formulations of the discontinuous Galerkin method for diffusion equations. *Mathematical Models and Methods in Applied Sciences*, Vol. 13, No. 3, pp.395–413, 2003.
- [56] O. C. Zienkiewicz and R. L. Taylor. The finite element method. Volume 1: The basis. Butterworth-Heinemann, Oxford, 2000.
- [57] O. C. Zienkiewicz and R. L. Taylor. The finite element method. Volume 3: Fluid dynamics. Butterworth-Heinemann, Oxford, 2000.